

# Cauchy–Characteristic Evolution and Waveforms

Nigel T. Bishop,\* Roberto Gómez,† Paulo R. Holvorcem,‡<sup>1</sup> Richard A. Matzner,‡<sup>2</sup>  
Philippos Papadopoulos,§ and Jeffrey Winicour†

\**Department of Mathematics, Applied Mathematics and Astronomy, University of South Africa, P.O. Box 392, Pretoria 0001, South Africa;*

†*Department of Physics and Astronomy, University of Pittsburgh, Pittsburgh, Pennsylvania 15260;*

‡*Center for Relativity, University of Texas at Austin, Austin, Texas 78712-1081; and §Department of Astronomy and Astrophysics, The Pennsylvania State University, University Park, Pennsylvania 16802*

Received April 2, 1996; revised March 4, 1997

---

We investigate a new methodology for the computation of waves generated by isolated sources. This approach consists of a global spacetime evolution algorithm based on a Cauchy initial-value formulation in a bounded interior region and based on characteristic hypersurfaces in the exterior; we match the two schemes at their common interface. The characteristic formulation allows accurate description of radiative infinity in a compactified finite coordinate interval, so that our numerical solution extends to infinity and accurately models the free-space problem. The matching interface need not be situated far from the sources, the wavefronts may have arbitrary nonspherical geometry, and strong nonlinearity may be present in both the interior and the exterior regions. Stability and second-order convergence of the algorithms (to the exact solution of the infinite-domain problem) are established numerically in three space dimensions. The matching algorithm is compared with examples of both local and nonlocal radiation boundary conditions proposed in the literature. For linear problems, matching outperformed the local radiation conditions chosen for testing, and was about as accurate (for the same grid resolution) as the exact nonlocal conditions. However, since the computational cost of the nonlocal conditions is many times that of matching, this algorithm may be used with higher grid resolutions, yielding a significantly higher final accuracy. For strongly nonlinear problems, matching was significantly more accurate than all other methods tested. This seems to be due to the fact that currently available local and nonlocal conditions are based on linearizing the governing equations in the far field, while matching consistently takes nonlinearity into account in both interior and exterior regions. © 1997 Academic Press

---

## I. INTRODUCTION

We consider here the numerical treatment of asymptotically nondispersive waves generated by an isolated source. The mathematical idealization of this problem involves boundary conditions at infinity which ensure that the total energy and the energy loss by radiation are both finite.

<sup>1</sup> Present address: Departamento de Matemática, Instituto de Matemática, Estatística e Computação Científica, Universidade Estadual de Campinas, Campinas, SP 13081-970 Brazil.

<sup>2</sup> Orson Anderson Fellow, Los Alamos National Laboratory, 1996–1997.

These are the conditions responsible for the proper  $1/r$  asymptotic decay of the radiation fields. However, for practical purposes, in the computational treatment of such a system by a Cauchy initial-value problem, an outer boundary is artificially established at some large but finite distance lying in the wave zone, i.e., many wavelengths from the source. Some outgoing radiation condition is then imposed upon this boundary in an attempt to approximate the proper asymptotic behavior at infinity. The boundary condition may cause partial reflection of the outgoing wave back into the system [1–4], which contaminates the accuracy of the evolution and of the waveform determined at infinity. Furthermore, nonlinear wave equations often display backscattering effects in the radiation zone, so that it may not be correct to try to entirely eliminate incoming radiation from the numerical solution. The errors introduced in this way are of an analytic origin, essentially independent of the computational discretization. In general, a systematic reduction of the error can be achieved only by simultaneously refining the discretization and moving the computational boundary to a larger radius, which is computationally very expensive for three-dimensional simulations. In this work we investigate a new approach, which does not introduce error at the analytic level.

For linear wave problems, a variety of approaches have been proposed for the treatment of the artificial boundary in steady-state, time-periodic, and truly time-dependent (nonstationary) situations. In this section we review only time-dependent ABC's in nondispersive situations (typified by the linear wave equation in three space dimensions); the reader is referred to recent reviews [4–7] for a general discussion of ABC's. During the past two decades, local ABC's in differential form have been extensively employed by several authors [1, 3, 8–12] with varying success. Some of these conditions can be derived as local approximations to exact integral representations of the solution in the exterior of the computational domain [8], while others are based on approximating the dispersion relation of the so-

called one-way wave equations [1, 10]. Higdon [3] showed that this last approach is essentially equivalent to specifying a finite number of angles of incidence for which the ABC's yield perfect transmission. Local ABC's have also been derived for the linear wave equation by considering the asymptotic behavior of outgoing solutions [9]; this kind of approach may be regarded as a generalization of the Sommerfeld outgoing radiation condition. Although such ABC's are relatively simple to implement and have a low computational cost (in a three-dimensional problem with  $O(N^3)$  interior grid points, their cost is  $O(N^2)$  per time step), their final accuracy is often limited because the simplifying assumptions they make about the detailed behavior of the wave fields are rarely met in practice [5, 6]. In general, systematic improvement can be achieved only with local conditions by moving the computational boundary to a larger radius, which is computationally expensive, especially for three-dimensional simulations.

The above disadvantages of local ABC's have led some workers to consider the actual implementation of exact nonlocal boundary conditions based on integral representations of the infinite-domain problem [5, 6, 13]. Even for problems where Green's function is known and easily computed, such approaches were initially dismissed as impractical [8]; however, the rapid increase in computer power has made it possible to implement exact nonlocal ABC's for the linear wave equation even in three space dimensions [14]. If properly implemented, this kind of method can yield numerical solutions which converge to the exact infinite-domain problem as the grid spacing and time step are decreased, keeping the artificial boundary at a fixed distance. However, due to nonlocality, the computational cost per time step usually grows at a higher power of grid size ( $O(N^4)$  per time step in three dimensions) than in a local approach [5, 6, 14], which in multidimensional problems may be very demanding even for today's supercomputers. Further, the applicability of current nonlocal ABC's is restricted to linear problems or to nonlinear solutions where nonlinearity may be neglected in the exterior domain [6].

To date, only a few works have been devoted to the development of ABC's for strongly nonlinear problems [5]. Thompson [15] generalized a previous nonlinear ABC of Hedstrom [16] to treat one- and two-dimensional problems in gas dynamics. These boundary conditions performed poorly in some situations because of their difficulty in adequately modeling the field outside the computational domain [5, 15]. Hagstrom and Hariharan [17] seem to have solved the above difficulties in one-dimensional gas dynamics problems by a clever use of Riemann invariants. These authors proposed a heuristic generalization of their local ABC's to three space dimensions, but to our knowledge it has not yet been implemented.

In practice, nonlinear problems are often treated by linearizing the governing equations in the far field and using either local or nonlocal ABC's [6, 7]. Besides introducing an approximation at the analytical level, this procedure requires that the artificial boundary be placed sufficiently far from the strong-field regions, which may sharply increase the computational cost in multidimensional simulations. There seems to be in the literature no method currently available which is able to produce numerical solutions which converge (as the discretization is refined) to the infinite-domain exact solution of a strongly nonlinear wave problem in multidimensions, keeping the artificial boundary at a fixed location which may be inside the strong-field region.

However, in this paper we propose, implement, and test such a numerical method for asymptotically nondispersive wave equations. Our method employs only local algorithms, but computes the entire solution to free-space infinity with effort  $O(N^3)$  per time step. The cost of the boundary treatment is larger than that of local ABC's, but is still  $O(N^2)$  per time step. In practice, using our algorithm increases the total computational cost by a factor of  $\sim 2$  with respect to a pure Cauchy algorithm with a local ABC.

In problems where the wave propagation is asymptotically nondispersive at large distances from the sources, the use of numerical methods based on a characteristic initial-value formulation [18] instead of the Cauchy formulation can effectively remove the above difficulties associated with computational boundaries at a finite distance. In these methods, four-dimensional spacetime is foliated along a family of outgoing characteristic hypersurfaces, with the evolution proceeding from one hypersurface to the next by an outward radial march which takes into account nonspherical and nonlinear effects in a consistent way [19]. There is no need to truncate spacetime at a finite distance from the sources, since compactification of the radial coordinate [20] makes it possible to cover the whole spacetime with a finite computational grid. In this way, the true radiation zone waveform may be directly computed by a finite-difference algorithm. Although the characteristic formulation may suffer from severe stability limitations in strong-field interior regions (where the characteristic hypersurfaces may develop caustics) [21], it proves to be both accurate and computationally efficient in the treatment of exterior, caustic-free regions [19].

Here we present a detailed study of a new approach which is free of error at the analytic level. It is based on a matched Cauchy-characteristic numerical evolution [22–25] (see also [26, 27] for matching a numerical Cauchy evolution to a perturbative characteristic solution). The characteristic algorithm provides an *outer* boundary condition for the interior Cauchy evolution, while the Cauchy algorithm supplies an inner boundary condition for the characteristic evolution. While previous implementations

of matching algorithms have focused on low-dimensional problems involving scalar [24, 28] and gravitational radiation [29, 30], here we present two new formulations of matching for three-dimensional scalar radiation, and systematically study their stability and accuracy. Since our matching algorithms consist of discretizations of an exact analytic treatment of the radiation from source to radiative infinity, they generate numerical solutions which converge to the exact analytic solution of the radiating system, even in the presence of strong nonlinearity. Thus, any desired accuracy to the free-space solution can be achieved by refining the grid, without moving the matching boundary. We show below that our method performs extremely well, even at moderate resolutions.

Our model radiating system is the wave equation for a scalar field  $\phi(x, y, z, t)$ ,

$$c^{-2}\partial_{tt}\phi = \nabla^2\phi + F(\phi) + S(x, y, z, t), \quad (1.1)$$

with nonlinear self-coupling  $F(\phi)$  and external source  $S$ . In principle, we need only require that  $F(\phi)$  derive from a stable potential. However, for our approach to be computationally efficient, it is important that the field decay as  $1/r$  along the outgoing characteristics [19]. This rules out fields with nonzero rest mass,  $F \sim \phi$ , which decay exponentially along the characteristics. Also, while we assume that  $c = \text{const.}$  here, the matching techniques we describe could be adapted to accommodate a variable  $c$ , provided that  $c$  approaches a constant value far from the sources. In the following we choose units so that  $c = 1$ .

In the standard computational implementation of the Cauchy problem for (1.1), initial data  $\phi(x, y, z, t_0)$  and  $\partial_t\phi(x, y, z, t_0)$  are assigned and evolved in some bounded spatial region, with some linear ABC imposed at the computational boundary. In a characteristic initial-value formulation (1.1) is expressed in standard spherical coordinates  $(r, \theta, \varphi)$  and a retarded time coordinate  $u = t - r$ ,

$$2\partial_{ur}g = \partial_{rr}g - \frac{L^2g}{r^2} + r(F + S), \quad (1.2)$$

where  $g = r\phi$  and  $L^2$  is the angular momentum operator

$$L^2g = -\frac{\partial_\theta(\sin\theta\partial_\theta g)}{\sin\theta} - \frac{\partial_{\varphi\varphi}g}{\sin^2\theta}. \quad (1.3)$$

The initial data are now  $g(r, \theta, \varphi, u_0)$ , on an initial outgoing characteristic cone  $u = u_0$ . (Since (1.2) is first order in  $u$ ,  $\partial_u g$  is not part of the initial data.)

In our matching implementations, (1.1) is integrated in an interior region  $r \leq R_m$  using a Cauchy algorithm, while a characteristic algorithm integrates (1.2) for  $r \geq R_m$ . The matching procedures ensure that, in the continuum limit,

$\phi$  and its normal derivative are continuous across the interface  $r = R_m$ . This is clearly a requirement for any consistent matching algorithm, since any discontinuity in the field or its derivatives at  $r = R_m$  could act as a spurious boundary source, contaminating both the interior and the exterior evolutions.

We begin our presentation in Section II with a discussion of a matching scheme based entirely on inter-grid interpolation procedures. The scheme is first introduced for spherically symmetric problems, and then generalized to three dimensions. In the three-dimensional algorithm, the characteristic evolution is carried out on an exterior spherical grid, while the Cauchy evolution uses a Cartesian grid covering the interior spherical region. Although a spherical grid could also be used in the interior, a Cartesian grid has the advantage that it does not require the use of special numerical procedures near the coordinate singularity at the origin. The use of a Cartesian discretization in the interior and a spherical discretization in the exterior makes the treatment of the interface somewhat more involved; in particular, guaranteeing the stability of the matching algorithm requires careful attention to the details of the inter-grid matching. Nevertheless, we find a reasonably broad range of discretization parameters for which our matching scheme is stable.

In Section III we discuss a different class of three-dimensional matching schemes, in which the continuity requirements for the field at the Cauchy-characteristic interface are employed in a form which may be regarded as an exact generalization of the Sommerfeld radiation condition. We exploit this formal similarity to discretize the continuity conditions in a stable way by using generalizations of well-known stable finite-difference schemes commonly used with radiation boundary conditions. In Section IV we demonstrate in a series of systematic numerical experiments that the matching algorithms introduced in Sections II and III provide global second-order accurate approximations to the solution of three-dimensional initial-value problems involving (1.1), in both linear and nonlinear situations. The matching algorithms are also compared to local and nonlocal ABCs proposed in the literature. We end with conclusions in Section V.

## II. MATCHING ALGORITHMS BASED ON INTER-GRID INTERPOLATIONS

### A. The Spherically Symmetric Case

We begin with the simple case of a spherically symmetric wave equation with no self-coupling ( $F = 0$ ). With the substitution  $G = r\phi$  and the use of spherical coordinates, (1.1) reduces to the one-dimensional wave equation

$$\partial_{tt}G = \partial_{rr}G + rS(r, t). \quad (2.1)$$

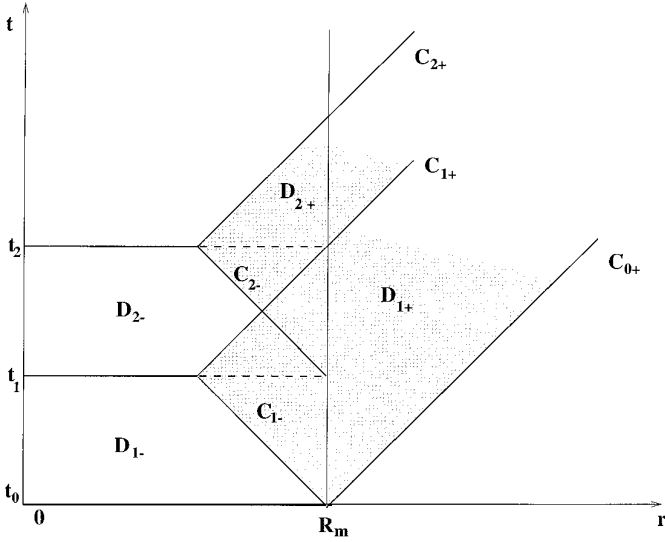


FIGURE 1

Consider initial Cauchy data  $G(r, t_0)$  and  $\partial_t G(r, t_0)$  in the region  $0 \leq r \leq R_m$ . Together with the regularity condition  $G(0, t) = 0$ , these data determine a unique solution in the domain of dependence  $D_{1-}$  indicated in Fig. 1. The outer boundary of the domain of dependence is the ingoing radial characteristic  $C_{1-}$  described by  $r = R_m - t + t_0$ . Although the source  $S$  is known for all times in the region  $r \leq R_m$ , the solution cannot be constructed throughout this domain. The complete solutions in the interior region  $r \leq R_m$  requires additional information, which can be furnished by giving the value of  $G$  on the outgoing characteristic  $C_{0+}$  described by  $r = R_m + t - t_0$  (see Fig. 1). In terms of the coordinates  $u = t - r$  and  $r$ ,  $C_{0+}$  is described by  $u = t_0 - R_m$ . In these coordinates, expressing  $g(r, u) = G(r, u + r)$ , the spherical wave equation takes the form

$$2\partial_{ur}g = \partial_{rr}g + rS. \quad (2.2)$$

A unique solution of (2.2) can be determined from the characteristic initial data consisting of  $g$  on  $C_{0+}$  and of the value of  $g$  on the characteristic  $C_{1-}$ . These data determine the solution uniquely throughout the future of  $C_{1-}$  and  $C_{0+}$ , the region  $D_{1+}$  in Fig. 1.

The matching scheme proceeds as shown in Fig. 1. First, initial Cauchy data are evolved from  $t_0$  to  $t_1$  throughout the region  $D_{1-}$ , which is in its domain of dependence. Next, the characteristic data induced on  $C_{1-}$  are combined with the initial characteristic data on  $C_{0+}$  to carry out a characteristic evolution throughout the region  $D_{1+}$ , bounded from the future by the characteristic  $C_{1+}$ . The solution determined from this initial stage induces Cauchy data at time  $t_1$  in the region  $r \leq R_m$ , inside the matching boundary.

This process can then be iterated to carry out the entire future evolution of the system.

Our matching algorithms are based upon a discretized version of this scheme in which the crisscross pattern of characteristics inside the radius  $R_m$  is at the scale of a grid spacing. The evolution algorithm consists of the following steps (see Fig. 2):

*Step 1. Cauchy Evolution.* The interior integration scheme is implemented on a uniform spatial grid  $r_i = i\Delta r$  ( $0 \leq i \leq M$ ) with outer radius  $R_B = M\Delta r$ . We discretize (2.1) using the standard second-order finite-difference scheme

$$\frac{G_i^{n+1} - 2G_i^n + G_i^{n-1}}{(\Delta t)^2} = \frac{G_{i+1}^n - 2G_i^n + G_{i-1}^n}{(\Delta r)^2} + r_i S_i^n, \quad (2.3)$$

where  $G_i^n = G(r_i, t_n)$ ,  $S_i^n = S(r_i, t_n)$ , and  $t_n = t_0 + n\Delta t$ . The interior evolution is initialized by evaluating  $G_i^0$  and  $G_i^1$  ( $0 \leq i \leq M$ ) to second order from the Cauchy initial data. In the  $n$ th time step, (2.3) is used to compute  $G_i^{n+1}$ ,  $1 \leq i \leq M$ , in terms of field values  $G_i^{n-1}$  and  $G_i^n$ . The regularity of  $\phi$  at  $r = 0$  implies that  $G_0^n = 0$  for all  $n$ . The boundary values  $G_{M+1}^n$  which are required by (2.3) are supplied by the matching procedure (Step 3).

*Step 2. Characteristic Evolution.* The characteristic algorithm is implemented on a uniform grid based on the dimensionless compactified radial coordinate

$$\eta = 1 - \frac{1}{1 + r/R_m}, \quad (2.4)$$

so that points at radiative infinity (corresponding to  $\eta = 1$ ) are included in the grid. (More generally, the numerical scheme could be implemented using any radial coordinate  $\eta$  which behaves as  $\text{const.} + O(r^{-1})$  as  $r \rightarrow \infty$ .) In order to prepare for the problem of matching an interior Cartesian grid to an exterior spherical grid, it is convenient to introduce a small gap between the outer radius  $R_B$  of the Cauchy grid and the matching radius  $R_m$  (which is also the inner radius of the characteristic grid). Although in spherical symmetry the algorithm may be simplified by taking  $R_B = R_m$  (so that the Cauchy and characteristic grids share a common boundary point), in three-dimensional Cartesian-spherical matching the outermost Cauchy grid points and the innermost characteristic grid points are necessarily distinct. For this reason, we study here the case of a finite gap  $R_m - R_B = \kappa\Delta r$ , where  $\kappa \geq 0$  is an arbitrary parameter. The characteristic grid consists of the uniformly spaced points  $\eta_\alpha = \frac{1}{2} + \alpha\Delta\eta$  ( $0 \leq \alpha \leq N_\eta$ ), where  $\Delta\eta = (2N_\eta)^{-1}$ . The retarded time levels  $u = u_n$  for the characteris-

tic evolution are chosen so that  $u = u_n$  intersects the time level  $t = t_n$  of the Cauchy evolution at the matching radius; therefore,  $u_n = t_n - R_m$  and  $\Delta u = \Delta t$ . We denote by  $g_\alpha^n$  the value of  $g$  at  $\eta = \eta_\alpha$ ,  $u = u_n$ . The initial characteristic data consist of  $g_\alpha^0$ ,  $0 \leq \alpha \leq N_\eta$ .

In the  $n$ th iteration of the evolution, we compute the field values at the grid points with  $u = u_n$  using the values of  $g_\alpha^{n-1}$ , which are known either from initialization or from the previous iteration. This is done by an outward marching algorithm with second-order global accuracy [19], whose generic radial step is based on the integral identity

$$g_Q = g_P + g_S - g_R + \frac{1}{2} \int_{PQRS} \psi \frac{du dr}{r^2} \quad (2.5)$$

( $\psi \equiv r^3 S$ ), which results when (2.2) is reexpressed in terms of variables  $u = t - r$ ,  $v = t + r$ , and then integrated over

the parallelogram  $PQRS$  of Fig. 3. For greater accuracy of the scheme, the ingoing characteristics  $PR$  and  $QS$  are chosen symmetrically around the radial grid points  $\eta = \eta_{\alpha-1}$  and  $\eta = \eta_\alpha$ , i.e.,

$$\eta_{\alpha-1} - \eta_P = \eta_R - \eta_{\alpha-1}, \quad \eta_\alpha - \eta_Q = \eta_S - \eta_\alpha. \quad (2.6)$$

The discretization of (2.5) involves (a) approximating the positions of  $P$ ,  $Q$ ,  $R$ , and  $S$  through

$$\eta_R = \eta_{\alpha-1} + \frac{\Delta t}{4R_m} (1 - \eta_{\alpha-1})^2 + O(\Delta t^3/R_m^3)$$

and similar expressions for the other corners, (b) replacing  $g_Q$ ,  $g_P$ , etc., in (2.5) by linear interpolates using data at adjacent radial grid points at the same retarded time, and

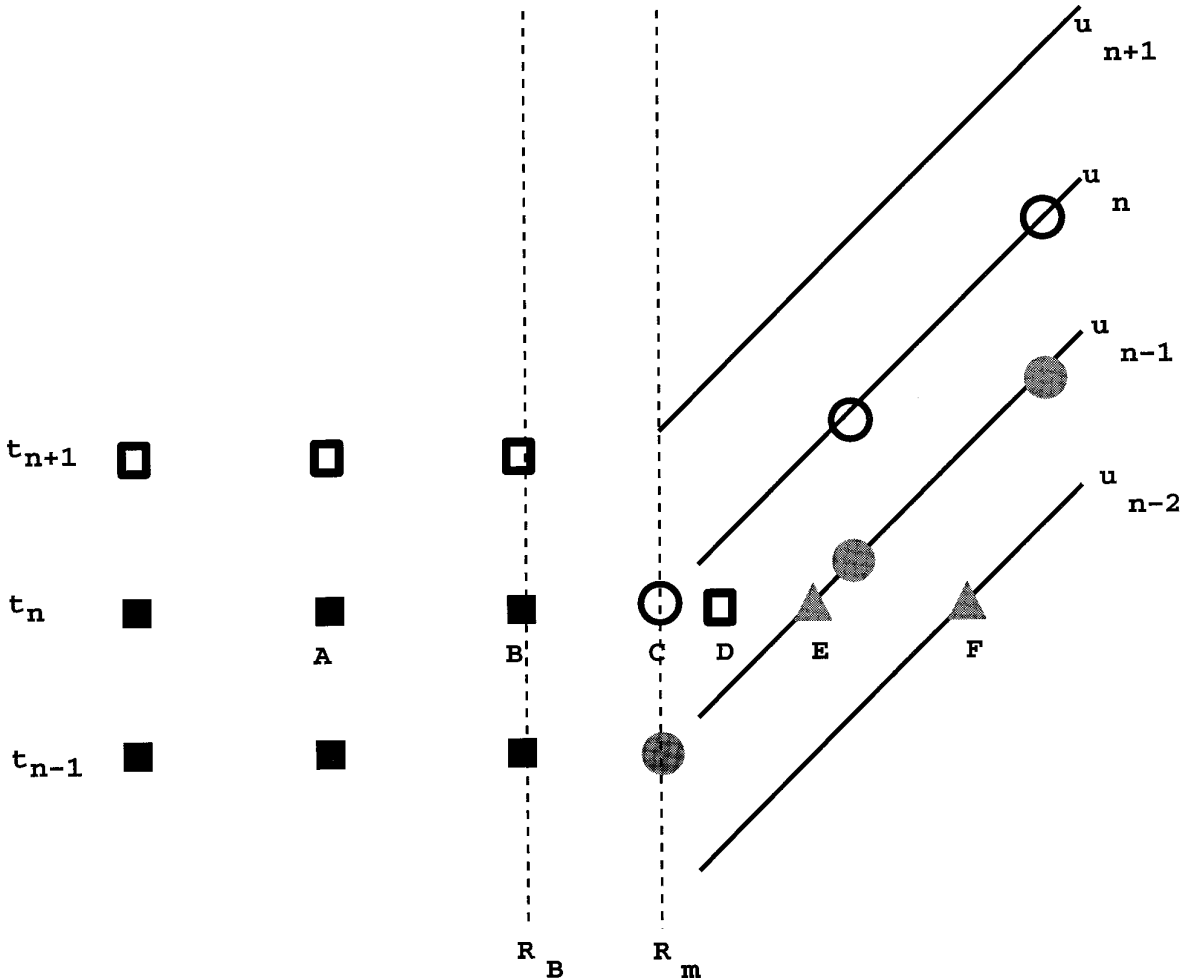


FIGURE 2

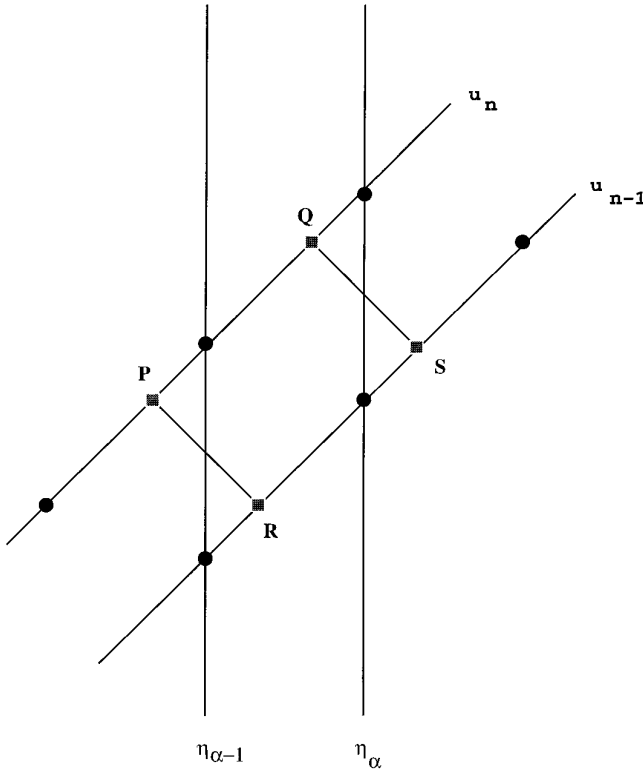


FIGURE 3

(c) approximating the integral term in (2.5) by the simple quadrature rule

$$\begin{aligned} \int_{PQRS} \psi \frac{du dr}{r^2} &= \int_{PQRS} \psi \frac{du d\eta}{\eta^2} \approx \frac{1}{2} \left( \frac{\psi_{\alpha-1}^{n+1}}{\eta_{\alpha-1}^2} + \frac{\psi_{\alpha}^n}{\eta_{\alpha}^2} \right) \int_{PQRS} du d\eta \\ &\approx \frac{1}{2} \Delta t \Delta \eta \left( \frac{\psi_{\alpha-1}^{n+1}}{\eta_{\alpha-1}^2} + \frac{\psi_{\alpha}^n}{\eta_{\alpha}^2} \right). \end{aligned} \quad (2.7)$$

With these approximations, (2.5) can be solved for  $g_{\alpha}^n$  in terms of previously computed field values  $g_{\alpha-1}^n$ ,  $g_{\alpha-2}^n$ ,  $g_{\alpha-1}^{n-1}$ ,  $g_{\alpha}^{n-1}$ , and  $g_{\alpha+1}^{n-1}$ . The resulting scheme can be applied even at radiative infinity ( $\alpha = N_{\eta}$ ), provided that  $\psi$  approaches a constant value as  $r \rightarrow \infty$  along characteristics  $u = \text{const}$ .

At the inner boundary of the characteristic grid ( $\alpha = 1$ ), the previous scheme must be slightly modified, since  $g_{\alpha-2}^n$  is not defined. For this special step,  $PQRS$  is chosen so that  $\eta_P = \eta_0$ ,  $\eta_Q = \eta_1$ , and  $g_R, g_S$  are approximated by quadratic interpolation in terms of  $g_0^{n-1}, g_1^{n-1}, g_2^{n-1}$ , which have already been computed. Besides these field values, the final evaluation of  $g_1^n$  still requires the value of  $g_0^n$ , which is supplied by the matching procedure (Step 3).

*Step 3. Matching.* Numerous schemes are possible in the case of spherically symmetric matching. Here we pre-

sent one which is stable for a wide range of gap sizes,  $0 \leq \kappa \leq 2$ . It provides the basis for the more complicated situation with an interior Cartesian grid and an exterior spherical grid, treated in the next subsection.

The required boundary values  $G_{M+1}^n$  and  $g_0^n$  are computed by a cubic radial interpolation at constant  $t$ , using the field values at points  $A, B, E$ , and  $F$  in Fig. 2. The first two of these field values are already known at the  $n$ th step, while the last two can be obtained by cubic radial interpolations along the previously evolved characteristics  $u = u_{n-1}$  and  $u = u_{n-2}$ , respectively. At the initial step, point  $F$  lies on the characteristic  $u = u_{-1} = -\Delta t - R_m$ , which is not evolved by the algorithm; we assume that this field value is supplied along with the initial data. Once the Cauchy and characteristic boundary values are computed, a new iteration may be performed starting from Step 1 above.

Since all the interpolations employed in the matching step have fourth-order error, we expect the whole matching algorithm to have the same second-order global accuracy exhibited by the separate Cauchy and characteristic algorithms. Numerical tests confirm this global second-order convergence.

### B. The Three-Dimensional Case

In three dimensions, we assume that the matching surface is again a sphere of fixed radius  $R_m$ , centered at the origin of the Cartesian coordinates  $(x, y, z)$ . This aligns the matching surface with the radial coordinate levels of the characteristic coordinate system  $(u, r, \theta, \varphi)$ . A characteristic evolution algorithm is used in the external region, which comprises the region of spacetime between  $r = R_m$  and radiative infinity. Cartesian coordinates  $(t, x, y, z)$  are used in the interior region, where the field  $\phi$  is evolved using the standard second-order explicit finite-difference representation of the wave equation (three-dimensional version of Eq. (2.3)).

We employ a uniform Cartesian grid which is contained in the cube  $-a \leq x, y, z \leq a$ . Each Cartesian direction is discretized using the grid points

$$\begin{aligned} x_i &= -a + (i-1)h, & y_j &= -a + (j-1)h, \\ z_k &= -a + (k-1)h \end{aligned}$$

( $1 \leq i, j, k \leq 2M$ ), where  $h = 2a/(2M-1)$ . The inner boundary of the characteristic grid is a spherical shell of radius  $R_m = a - h/2$ , centered at the origin of Cartesian coordinates. Cartesian grid points are classified depending on their location with respect to the spherical shell  $r = R_m$  as follows: (a) an *interior point* is one for which  $x_i^2 +$

$y_j^2 + z_k^2 < R_m^2$ ; (b) the remaining grid points are called *exterior points*; and (c) an interior point which has at least one exterior nearest neighbor is called an *interior boundary point*.

The characteristic integration of the wave equation (1.2) is conceptually close to the one-dimensional problem. The nonzero angular momentum introduces a term ( $L^2g/r^2$ ), which couples the evolution of neighboring angles. The nonlinear term can also be regarded as an effective source term. As before, the wave equation (1.2) can be integrated to yield an identity of the form (2.5), where  $\psi$  is now defined as

$$\psi = -L^2g + r^3[S + F(g/r)]. \quad (2.8)$$

The new integral identity is valid for any angular direction, and may be used as an outward marching algorithm by making the same approximations which were discussed above in the spherically symmetric case. Here we again assume that  $\psi$  approaches a constant value as  $r \rightarrow \infty$  at constant  $u, \theta, \phi$ ; this will be satisfied for smooth asymptotically nondispersive waves (for which  $g$  and  $L^2g$  are both finite at radiative infinity), provided that the source term  $S$  decays fast enough along characteristic surfaces and the nonlinear term  $F(\phi)$  satisfies the restrictions discussed in Section I.

The numerical evaluation of the angular momentum term  $L^2g$  requires finite-differencing in the angular directions. Although the simplest approach here would be to use a latitude–longitude grid, the presence of a coordinate singularity at the poles  $\theta = 0, \pi$  would severely limit the range of time steps for which the characteristic algorithm is stable. For this reason, we adopt a two-patch parameterization of the unit sphere in terms of stereographic coordinates [31, 32]  $\zeta_{\pm} = [\tan(\theta/2)]^{\pm 1} e^{\pm i\phi}$ , where the upper and lower signs are used to cover the hemispheres  $0 \leq \theta \leq \pi/2$  and  $\pi/2 \leq \theta \leq \pi$ , respectively. In terms of the real coordinates  $q_{\pm} = \text{Re } \zeta_{\pm}$  and  $p_{\pm} = \text{Im } \zeta_{\pm}$ , the two patches are described by the inequalities  $|q_{\pm}| \leq 1, |p_{\pm}| \leq 1$  (so that the two patches have a slight overlap around  $\theta = \pi/2$ ), and the angular momentum operator takes the form

$$L^2g = -\frac{1}{4}(1 + q^2 + p^2)^2[\partial_{qq} + \partial_{pp}]g, \quad (2.9)$$

which is valid in both patches. The above expression is discretized using second-order centered differences on the uniform grid

$$q_k = k \Delta s, \quad p_l = l \Delta s \quad (-N_s \leq k, l \leq N_s), \quad (2.10)$$

where  $\Delta s = 1/N_s$ .

The introduction of two patches implies that a special computation is necessary at the boundaries of each patch. For example, the evaluation of the angular momentum

operator at a patch boundary by means of a centered difference scheme requires information which may be obtained from the other patch, using one of several possible interpolation schemes [31]. The main requirement for the interpolation procedure is that the accuracy of the resulting values be sufficient for the consistent convergence of the discretized version of  $L^2$  throughout the patch. In this case, the use of an interpolation scheme with  $O((\Delta s)^4)$  error preserves the second-order global accuracy of the characteristic algorithm.

By comparing the physical and numerical domains of dependence, it can be shown that the local Courant–Friedrichs–Lewy (CFL) conditions for the characteristic evolution are

$$\begin{aligned} \Delta u &\leq 2 \Delta r, \\ \Delta u &\leq -\Delta r + \left[ \Delta r^2 + \left( \frac{2r \Delta s}{1 + q^2 + p^2} \right)^2 \right]^{1/2}, \end{aligned} \quad (2.11)$$

where  $\Delta r$  is the radial grid spacing at radius  $r$ . The last condition is strongest when  $|q| = 1, |p| = 1$ , i.e., at the regions within each patch where the stereographic grid is most dense.

The three-dimensional matching procedure is schematically illustrated in Fig. 4. For each interior boundary point  $B$ , we determine its nearest neighbors on the Cartesian

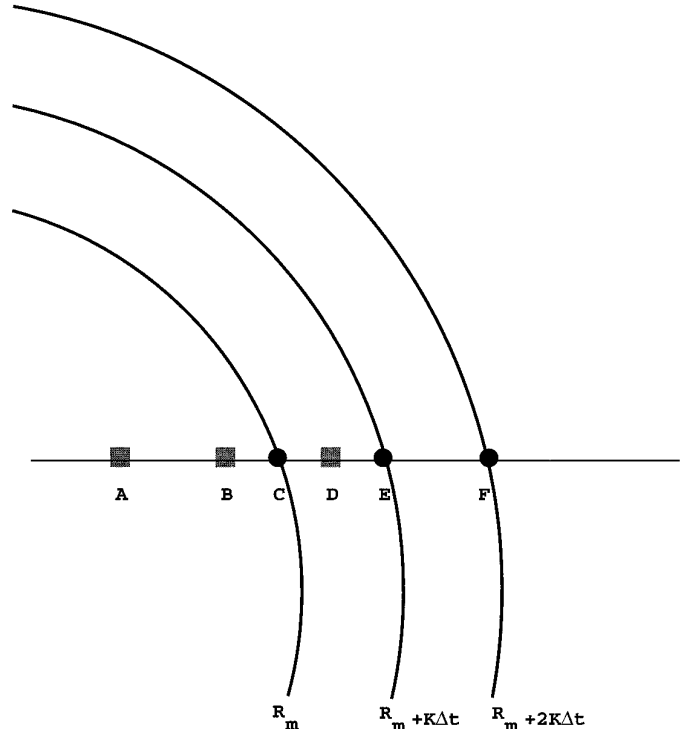


FIGURE 4

grid. For each nearest neighbor  $D$  which is an exterior point, we identify the nearest neighbor  $A$  which is symmetric to  $D$  with respect to  $B$ . Points  $C$ ,  $E$ , and  $F$  are then determined by the intersection of the line  $AB$  with the spherical shells of radius  $r = R_m$ ,  $r = R_E = R_m + K \Delta t$ , and  $r = R_F = R_m + 2K \Delta t$ , respectively, where the new parameter  $K$  is taken to be a positive integer (the choice of  $K$  is discussed later in this section). We may note the analogy between points having the same labels in Figs. 4 and 2: the field values at points  $E$  and  $F$  may again be obtained by interpolation along previously evolved characteristic cones, while the field values at  $C$  and  $D$ , obtained by cubic interpolation from  $A$ ,  $B$ ,  $E$ , and  $F$ , yield boundary values for the characteristic and Cauchy evolutions, respectively. The separation between  $B$  and  $C$ , which varies from boundary point to boundary point, is analogous to the finite “gap” introduced in the spherically symmetric algorithm.

Despite the above close analogy, the three-dimensional implementation requires some additional field interpolations which are not needed in spherical symmetry.

First, the set of field values at the points labeled  $C$  in Fig. 4 lie at the intersections of the sphere  $r = R_m$  with Cartesian coordinate lines, and must therefore be interpolated onto the stereographic grid used by the characteristic scheme. Given a characteristic grid point  $C'$  on the sphere described by  $t = t_n$ ,  $r = R_m$ , we determine the Cartesian direction ( $x$ , say) which is closest to radial at  $C'$ . We locally parameterize the sphere near  $C'$  by the Cartesian coordinates ( $y$ ,  $z$ ), and then use the field values at the intersections of the sphere with  $x$  coordinate lines to evaluate the field at  $C'$  through bi-cube interpolation in ( $y$ ,  $z$ ). A detailed analysis shows that the  $4 \times 4$  stencil used in this interpolation will always be properly contained in the projection of the sphere on the ( $y$ ,  $z$ ) plane provided that the Cartesian grid size  $2M$  is greater than 21.

Second, the field values at the points  $E$  and  $F$  of Fig. 4 need to be computed by interpolating in both the radial and the angular directions along suitable characteristic cones. In practice, whenever the evolution of a new characteristic cone  $u = u_n$  is completed, we perform cubic radial interpolations to evaluate the field over the spheres described by  $u = u_n$ ,  $r = R_E$  and  $u = u_n$ ,  $r = R_F$ . These field values, which lie on the stereographic grid, are stored for  $K$  and  $2K$  time steps, respectively, until they become necessary to compute boundary values for both grids. At this point, the field values at  $E$  and  $F$  are computed from the stored data through bi-cubic interpolation in stereographic coordinates.

There is one ambiguity that must be resolved before the computed field value at  $D$  ( $\phi_D$ ) can be used in the Cauchy evolution. For some points  $D$ ,  $\phi_D$  may be calculated in more than one way. As shown in Fig. 5, the point  $D$  may be an exterior point which is a nearest neighbor to two distinct interior boundary points  $B$  and  $B'$ . In such cases

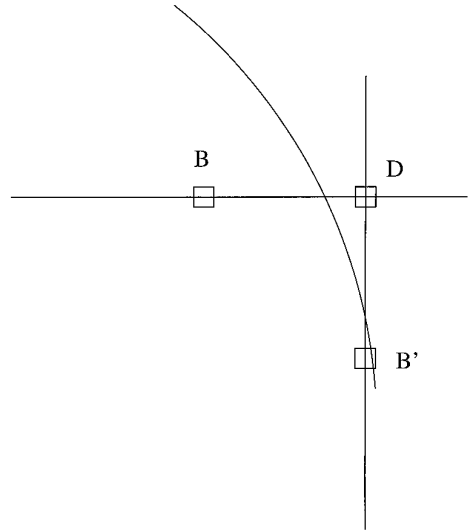


FIGURE 5

we choose for  $\phi_D$  the value obtained by interpolation along the Cartesian direction which is closest to the local radial direction; in Fig. 5, this would be the line  $BD$ .

Once the above process is completed, the field is known at all Cauchy and characteristic boundary points, so that the interior and exterior algorithms can advance by one time step. The cubic polynomials used in the boundary interpolations are sufficiently accurate to preserve the global second-order accuracy of the Cauchy and characteristic algorithms.

We now discuss the choice of the parameter  $K$  introduced above. Numerical experimentation with several values of  $K$ ,  $\Delta t$ , and  $h$  reveals that the above algorithm always becomes unstable when the ratio  $K \Delta t/h$  is sufficiently small. An intuitive explanation for this behavior could be that, when  $K \Delta t \ll h$ , the boundary point  $D$  in Fig. 4 would be updated by extrapolation rather than interpolation, thereby making the matching scheme prone to instabilities. However, since the spherically symmetric matching scheme (which is analogous to the three-dimensional scheme with  $K = 1$ ) was found to be stable for all sufficiently small  $\Delta t$ , it seems likely that the instabilities observed in the three-dimensional scheme are also related to the two-dimensional interpolation procedures used to generate the field values at points  $E$  and  $F$  and to interpolate the field values at  $r = R_m$  onto the stereographic grid. In any case, we consider it safer to choose  $K$  so as to satisfy the condition  $2K \Delta t/h \geq 1$ , which ensures that the boundary points  $D$  are never updated by extrapolation. In practice, we take

$$K = [h/2 \Delta t] + 1, \quad (2.12)$$

where the brackets denote the integer part.



### III. MATCHING WITH GENERALIZED SOMMERFELD CONDITIONS<sup>3</sup>

Here we introduce an alternative formulation for Cartesian–spherical matching, which exhibits certain formal similarities with more traditional approaches based on the Sommerfeld radiation condition. Let us consider the identity obtained by differentiating the definition  $g = r\phi$  with respect to  $r$  at constant  $u$ , which may be written as

$$\partial_t \phi + \partial_r \phi + \frac{\phi}{r} = \frac{1}{r} \tilde{\partial}_r g, \quad (3.1)$$

where the two derivatives on the left-hand side are taken at constant  $r$  and  $t$ , respectively, and  $\tilde{\partial}_r = \partial_t + \partial_r$  denotes the radial derivative at constant  $u$ . The above identity is valid for arbitrary smooth wave motions, without any assumption concerning particular wavefront geometries, linearity, etc. Because of its similarity to the Sommerfeld radiation condition, we refer to (3.1) as a *generalized Sommerfeld condition*.

In a traditional approach involving a Cauchy evolution and artificial radiation boundary conditions, the inhomogeneous term  $\tilde{\partial}_r g$  in (3.1) is neglected, yielding the Sommerfeld radiation condition. The evolution algorithm resulting from the discretization of the wave equation in the interior and the Sommerfeld condition at the computational boundary would then converge to the exact solution of the initial-value problem only when the waves crossing the boundary are outgoing, linear, and spherically symmetric about  $r = 0$ .

On the other hand, in a matched algorithm it becomes possible to use (3.1) in its exact form, since the characteristic evolution can provide information for the discrete evaluation of  $\tilde{\partial}_r g$  at the matching surface. If, as is often the case, the wave motions being computed do not deviate too much from spherical symmetry, and if nonlinear effects are not too strong, we expect the right-hand side of (3.1) to be a small (exact) correction to the usual Sommerfeld condition. Alternatively, (3.1) can be regarded as a condition expressing the continuity of a derivative of the field across the matching surface. Clearly, this continuity property is essential to ensure that the matching algorithm is consistent with the free-space initial-value problem being solved, for an arbitrary choice of the matching interface.

The generalized Sommerfeld condition (3.1) is also attractive from the point of view of numerical stability. In fact, it is well known from the literature on absorbing boundary conditions [3, 4] that the homogeneous version of (3.1) may be discretized in a stable way, at least for simple boundary geometries. This suggests that, by choos-

ing a suitable discrete approximation to  $\tilde{\partial}_r g$ , the exact condition (3.1) might “inherit” the stability properties exhibited by its homogeneous counterpart. Our numerical experience with this class of matching algorithms (see Subsection IV.A) is consistent with this expectation.

The discretization of (3.1) at the boundary of the Cartesian grid would require that we rewrite the term  $\partial_r \phi$  as

$$\partial_r \phi = \frac{1}{r} (x \partial_x \phi + y \partial_y \phi + z \partial_z \phi). \quad (3.2)$$

If, as in the previous sections, the matching surface is taken to be a sphere  $r = \text{const.}$ , the required finite-difference replacements of (3.2) become quite complicated, involving a combination of centered and one-sided differences which varies from boundary point to boundary point. This difficulty may be avoided if we observe that the radial derivative at constant  $u$  used to obtain (3.1) is a particular example of a derivative taken along the tangent space to the characteristic cone  $u = \text{const.}$  which contains a given boundary point. Differentiating  $g = r\phi$  with respect to the Cartesian direction which is closest to the local radial direction (keeping  $u$  constant) should also generate a useful exact boundary condition, which would have the advantage of involving spatial derivatives with respect to a single Cartesian direction [3]. If this is taken as the  $x$  direction, then a simple calculation yields the generalized Sommerfeld condition

$$\partial_t \phi + \frac{r}{x} \partial_x \phi + \frac{\phi}{r} = \frac{1}{x} \tilde{\partial}_x g, \quad (3.3)$$

where  $\tilde{\partial}_x = (x/r)\partial_t + \partial_x$ . This condition may be discretized stably using one-sided differences in  $t$  and  $x$  (see Subsection III.B).

In the literature on artificial radiation boundary conditions, higher-order conditions are often employed as a means of reducing the amount of spurious back reflections at the computational boundary [3, 10]. In the context of Cauchy–characteristic matching, this motivates us to investigate the behavior of higher-order generalized Sommerfeld conditions. If (3.3) is differentiated with respect to  $x$  at constant  $u$ , we obtain the second-order exact boundary condition

$$\partial_t^2 \phi + \frac{2r}{x} \partial_{tx} \phi + \frac{r^2}{x^2} \partial_x^2 \phi + \frac{2}{x} \partial_x \phi + r \left( \frac{1}{x^2} + \frac{1}{r^2} \right) \quad (3.4)$$

$$\partial_t \phi + \left( \frac{1}{x^2} - \frac{1}{r^2} \right) \phi = \frac{r}{x^2} \tilde{\partial}_x^2 g;$$

<sup>3</sup>For downloadable codes, see <http://godel.ph.utexas.edu/Members/paulo/welcome.html> or its mirror <http://www.ime.unicamp.br/~holvorce/>.

a stable discretization of the above condition involves centered differences in  $t$  and one-sided differences in  $x$  (see Subsection III.B).

### A. Computational Grids

The matching algorithms based on generalized Sommerfeld conditions, to be presented in the next subsection, make use of a computational grid structure which differs slightly from that employed in the previously presented matching algorithms. Although both kinds of matching procedures could in principle be implemented on the same grids, the different grid structure presented here serves to illustrate the flexibility of implementation of Cauchy-characteristic matching.

In the algorithms of the next subsection, the interior region, of radius  $R_m$ , is discretized in Cartesian coordinates  $(x, y, z)$  with a grid of uniform spacing  $h = R_m/N$ . Specifically, the interior computational grid consists of those grid points

$$x_i = ih, \quad y_j = jh, \quad z_k = kh$$

whose distance to the origin is strictly less than  $R_m$ . The set of interior grid points may be expressed in the form

$$\mathcal{I} = \{(x_i, y_j, z_k); |i| \leq N-1, |j| \leq \rho_i, |k| \leq \sigma_{ij}\},$$

where  $\rho_i, \sigma_{ij}$  are nonnegative integers. At all points of  $\mathcal{I}$ , the wave equation is discretized employing centered, second-order finite differences in space and time. This in turn requires that the set of boundary points

$$\begin{aligned} \mathcal{B} = & \{(x_i, y_j, z_k); |i| \leq N-1, |j| \leq \rho_i, |k| = \sigma_{ij} + 1\} \\ & \cup \{(x_i, y_j, z_k); |j| \leq N-1, |k| \leq \rho_j, |i| = \sigma_{jk} + 1\} \\ & \cup \{(x_i, y_j, z_k); |k| \leq N-1, |i| \leq \rho_k, |j| = \sigma_{ki} + 1\} \end{aligned}$$

be also included in the computational grid. The field values at these points will be updated using discrete versions of the generalized Sommerfeld conditions.

The characteristic evolution is carried out in the region  $R_m \leq r \leq \infty$ , which is compactified using the radial coordinate  $\xi = r^{-1}$ . We choose uniformly spaced grid points in the  $(u, \xi)$  plane, given by

$$\begin{aligned} \xi_\alpha &= r_\alpha^{-1} = R_m^{-1} - \alpha \Delta \xi, \quad \alpha = 0, 1, \dots, N_\xi, \\ u_n &= n \Delta t - R_m, \quad n = 0, 1, 2, \dots, \end{aligned}$$

where  $\Delta \xi = (R_m N_\xi)^{-1}$  and  $\alpha = N_\xi$  corresponds to radiative infinity ( $\Delta t$  is the common time step of the Cauchy and characteristic evolutions). The values of  $u_n$  are chosen so that the  $n$ th characteristic cone  $u = u_n$  intersects the  $n$ th time level  $t_n = n \Delta t$  of the Cauchy evolution at  $r = R_m$  (Fig.

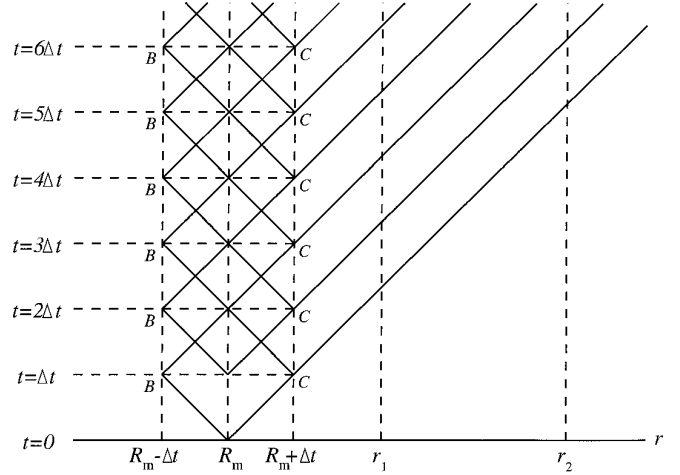


FIGURE 6

6). The boundary condition for the characteristic evolution should be provided at (or near)  $r = R_m$  by the Cauchy evolution. In the present scheme, we supply the boundary values at the grid points labeled  $B$  in Fig. 6, which are located at  $r = R_m - \Delta t$  along the characteristic cones  $u = u_n$ . (The  $B$  point at  $u = u_n$  is actually at the time level  $t = t_{n-1}$ ). In the algorithm to be described in the next subsection, we shall also need to approximate the value of the field at the points labeled  $C$  in Fig. 6, which are located at  $r = R_m + \Delta t$  along the characteristic cones  $u = u_n$ . (The  $C$  point at  $u = u_n$  lies at the  $t = t_{n+1}$  hypersurface.)

For the discretization of the angular directions, we adopt here a global approach based on “quasi-regular triangulations” of the unit sphere. Ideally, such a discretization would consist of a set of angular grid points

$$\mathcal{A} = \{(\theta_\beta, \varphi_\beta), \beta = 1, 2, \dots, N_{\text{ang}}\},$$

distributed so that the smallest angular separation between two grid points is as large as possible (i.e., so that  $\min_{\beta \neq \gamma} \Delta \theta_{\beta\gamma}$  is maximized, where  $\Delta \theta_{\beta\gamma}$  denotes the angular separation between  $(\theta_\beta, \varphi_\beta)$  and  $(\theta_\gamma, \varphi_\gamma)$ ). For particular small values of  $N_{\text{ang}}$ , the vertices of the five regular Platonic solids are examples of triangulations possessing this maximal property. For large  $N_{\text{ang}}$ , a quasi-regular triangulation has a sharply defined average angular spacing  $\Delta$  between nearest neighbors, and is essentially isotropic. Furthermore, its global nature does not require the use of two angular coordinate patches as in the discretization based on stereographic coordinates. Since the maximal property prevents the occurrence of very close pairs of angular grid points, it contributes to increase the range of time steps corresponding to stable characteristic evolution algorithms. In practice, we construct distributions of angular grid points which approximately satisfy the maximal prop-

erty. (See Appendix A for a discussion of techniques.) It should be noted that the matching algorithm to be described in the next subsection does not depend in any essential way on the use of quasi-regular triangulations. Other discretizations, such as the stereographic grids of Section II.B, can also be employed, with only minor changes in the algorithm.

### B. Matching Algorithm

In this section, we describe in detail the various steps of a matching algorithm based on generalized Sommerfeld conditions. In order to simplify the discussion, let us assume that both the Cauchy initial data ( $\phi$  and  $\partial_t \phi$  at  $t = 0$ ) and the external forcing  $S$  are identically zero for  $r \geq R_m - \Delta t$ , and that the characteristic initial data specify no incoming waves, that is,  $g = 0$  for  $u = u_0 = -R_m$ ,  $r \geq R_m$ . [These simplifying assumptions are not essential in the matching algorithm. Nonzero forcing terms in the exterior could be included in the  $\psi$  term defined in (2.8). The inclusion of characteristic initial data containing incoming waves would require a more elaborate scheme to compute the right-hand sides of the generalized Sommerfeld conditions during the first few time steps.] With these assumptions, it is easy to see that

$$g_{\alpha\beta}^0 = g_{\alpha\beta}^1 = 0$$

for  $\alpha = 0, 1, \dots, N_\xi$ ,  $\beta = 1, 2, \dots, N_{\text{ang}}$ , where  $g_{\alpha\beta}^n$  denotes the value of  $g$  at  $u = u_n$ ,  $\xi = \xi_\alpha$ ,  $\theta = \theta_\beta$ ,  $\varphi = \varphi_\beta$ . We must also initialize the field at the characteristic boundary points (Fig. 6) located at  $t = \Delta t$ , for each angular direction. Using the Cauchy initial data, we conclude that these field values may be initialized to zero with an error  $O(\Delta t^2)$ ; therefore we set

$$\tilde{g}_\beta^1 = 0, \quad 1 \leq \beta \leq N_{\text{ang}},$$

where  $\tilde{g}_\beta^n$  denotes the value of  $g$  at the characteristic boundary point  $t = n \Delta t$ ,  $r = R_m - \Delta t$ ,  $\theta = \theta_\beta$ ,  $\varphi = \varphi_\beta$ . The field values on the Cartesian grid  $\mathcal{S} \cup \mathcal{B}$  may also be initialized with second-order accuracy as

$$\begin{aligned} \phi_{ijk}^0 &= \phi(ih, jh, kh, 0), \\ \phi_{ijk}^1 &= \phi(ih, jh, kh, 0) + \Delta t \partial_t \phi(ih, jh, kh, 0), \end{aligned}$$

where  $\phi_{ijk}^n = \phi(ih, jh, kh, n \Delta t)$ . Note that in this process the boundary points of the Cartesian grid are initialized to zero.

In the  $n$ th iteration of the algorithm, we advance the Cauchy evolution from  $t = t_n$  to  $t = t_{n+1}$  and the characteristic evolution from  $u = u_n$  to  $u = u_{n+1}$ . This is done in the following steps:

*Step 1. Update the Interior Cartesian Grid Points.* As mentioned earlier, this step is performed using second-order centered differences in space and time. It is assumed that the required boundary values of  $\phi_{ijk}^n$  have been computed either from the previous steps or from initialization.

*Step 2. Update the Characteristic Grid Points.* We assume here that the field values  $\tilde{g}_\beta^n$ ,  $g_{\alpha\beta}^n$ , and  $g_{\alpha\beta}^{n-1}$  are available from previous iterations. The outward marching along the new characteristic cone  $u = u_{n+1}$  then proceeds by a second order algorithm which is analogous to that presented in Section II. We use different procedures to update the grid points at  $r = r_0 = R_m$  and at  $r = r_\alpha$ ,  $\alpha \geq 1$ .

The characteristic grid points at  $r = r_0$  are evolved by considering the characteristic parallelogram centered at  $r = R_m$ ,  $t = t_n$ , whose inner and outer corners are  $B$  ( $r = R_m - \Delta t$ ,  $t = t_n$ ) and  $C$  ( $r = R_m + \Delta t$ ,  $t = t_n$ ) (Fig. 6). Using the integral identity (2.5) with  $\psi$  given by (2.8) we can write, to fourth order in  $\Delta t$ ,

$$g_{0\beta}^{n+1} = \tilde{g}_\beta^n + g_C - g_{0\beta}^{n-1} - (\Delta t)^2 [R_m^{-2} L^2 g_{0\beta}^n - R_m F(R_m^{-1} g_{0\beta}^n)], \quad (3.5)$$

where  $g_C$  denotes the value of  $g$  at the point  $C$ . This value can be approximated by quadratic interpolation in  $\xi$  from the values of  $g_{0\beta}^{n-1}$ ,  $g_{1\beta}^{n-1}$ , and  $g_{2\beta}^{n-1}$ .

We now consider the evaluation of the angular momentum term  $L^2 g_{0\beta}^n$  appearing in (3.5). Let

$$(\theta_\gamma, \varphi_\gamma), \quad \gamma \in I \quad (3.6)$$

be the  $N_L$  nearest neighbors of  $(\theta_\beta, \varphi_\beta)$  on the chosen discretization of the unit sphere, where  $I \subset \{1, 2, \dots, N_{\text{ang}}\}$  and  $\beta \in I$ . A general finite-difference approximation to  $L^2 g_{\alpha\beta}^n$  using the stencil (3.6) may be written as

$$L^2 g_{\alpha\beta}^n = \Delta^{-2} \sum_{\gamma \in I} c_\gamma g_{\alpha\gamma}^n, \quad (3.7)$$

where  $\Delta$  is the average angular spacing of the discretization of the unit sphere, and  $c_\gamma$  are coefficients which remain bounded as  $\Delta \rightarrow 0$  (note that, since the angular discretization is not perfectly regular, a different set of coefficients  $c_\gamma$  must be used for each  $\beta$ ).

Among the many possible difference schemes of the form (3.7), we adopt here an approximation based on Hardy multiquadrics [33]. This kind of scattered data approximation often outperforms other existing methods [34], and has been successfully employed in the numerical solution of partial differential equations in fluid mechanics [35] and general relativity [35, 37]. All multiquadric approximations involve an arbitrary ‘‘shape parameter’’  $s$  [33], which is usually taken to be of the order of the grid

spacing [38, 39]. The main difficulties encountered in the use of multiquadrics are the lack of general criteria for the choice of  $s$  [40] and the fact that the convergence of this class of approximations has been studied only in a few idealized cases [38, 39]. In Appendix B, we present a general multiquadric technique which avoids both difficulties by applying certain corrections to the usual multiquadric approximations. In particular, this technique can generate finite-difference formulas of the form (3.7) with truncation error  $O(\Delta^p)$ , where the integer  $p$  is a selectable parameter. Moreover, the arbitrariness in the choice of the shape parameter  $s = s_L$  is reduced in the new technique, since it requires that  $s_L/\Delta = \text{const.}$  as  $\Delta \rightarrow 0$ . (It is generally satisfactory to fix this ratio at some value between 5 and 15). In the following, we assume that the truncation error of the formulas (3.7) is at least  $O(\Delta^2)$ .

In order to compute  $g_{\alpha\beta}^{n+1}$  ( $1 \leq \alpha < N_\xi$ ) from previously computed field values, we consider a characteristic parallelogram with corners  $P = (u_{n+1}, \xi_P)$ ,  $Q = (u_{n+1}, \xi_Q)$ ,  $R = (u_n, \xi_R)$ , and  $S = (u_n, \xi_S)$ , chosen so that

$$\xi_R - \xi_{\alpha-1} = \xi_{\alpha-1} - \xi_P, \quad \xi_S - \xi_\alpha = \xi_\alpha - \xi_Q.$$

The integral identity (2.5) is then applied, with the integral term approximated by a numerical quadrature rule of the form

$$\int_{PQRS} \psi \frac{du dr}{r^2} = \Delta t \Delta \xi (w_\alpha^{(1)} \psi_{\alpha-1}^{n+1} + w_\alpha^{(2)} \psi_\alpha^n + w_\alpha^{(3)} \psi_{\alpha-1}^n), \quad (3.8)$$

which can be evaluated using only previously computed field values. The quadrature weights in (3.8) are uniquely determined by the condition that the truncation error of the rule be  $O(\Delta t^3 \Delta \xi + \Delta t^2 \Delta \xi^2 + \Delta t \Delta \xi^3)$  as  $\Delta t, \Delta \xi \rightarrow 0$ . Since the points  $R$  and  $S$  lie in the previously evolved hypersurface  $u = u_n$ , the values of  $g_R$  and  $g_S$  can be obtained by quadratic interpolation in  $\xi$  from  $g_{\alpha-1,\beta}^n$ ,  $g_{\alpha\beta}^n$ , and  $g_{\alpha+1,\beta}^n$ . If  $\alpha \geq 2$ , the values of  $g_P$  and  $g_Q$  can be analogously interpolated from  $g_{\alpha-2,\beta}^{n+1}$ ,  $g_{\alpha-1,\beta}^{n+1}$ , and  $g_{\alpha\beta}^{n+1}$  (the first two of which have already been computed), so that (2.5) can be solved for  $g_{\alpha\beta}^{n+1}$ . In the special case  $\alpha = 1$ , we interpolate  $g_P$  and  $g_Q$  from  $\tilde{g}_\beta^n$ ,  $g_{\beta}^{n+1}$ , and  $g_{1\beta}^{n+1}$ , so that (2.5) can be solved for this latter quantity.

The updating of the grid points at radiative infinity ( $\alpha = N_\xi$ ) can be regarded as a limit of the above procedure as  $r_Q, r_S \rightarrow \infty$ . The values of  $g_P$  and  $g_R$  can be obtained by quadratic interpolation in  $\xi$  from data on the three outermost radial layers, while  $g_Q$  and  $g_S$  are grid values at infinity. Finally, the quadrature rule (3.8) can still be used, since both the weights and the function  $\psi$  approach finite limits as  $r_Q, r_S \rightarrow \infty$  (assuming that the nonlinear term satisfies the restrictions of Section I and the source term  $S$  vanishes for sufficiently large  $r$ ).

*Step 3. Update the Boundary Points of the Cartesian Grid.* At each boundary point  $(x_i, y_j, z_k) \in \mathcal{B}$ , the field is updated by a discrete version of either (3.3) or (3.4), with the spatial derivatives being taken along the Cartesian direction which is closest to the local radial direction. If the left-hand side of (3.3) is discretized using second-order one-sided differences in  $x$  and  $t$ , we obtain the updating scheme

$$\left( \frac{3}{2} + \frac{3\rho\tilde{r}_{ijk}}{2|i|} + \frac{\rho}{\tilde{r}_{ijk}} \right) \phi_{ijk}^{n+1} = 2\phi_{ijk}^n - \frac{1}{2} \phi_{ijk}^{n-1} + \frac{\rho\tilde{r}_{ijk}}{|i|} \left( 2\phi_{i\mp 1,jk}^{n+1} - \frac{1}{2} \phi_{i\mp 2,jk}^{n+1} \right) + \frac{\rho}{i} \tilde{\partial}_x g, \quad (3.9)$$

where  $\rho = \Delta t/h$ ,

$$\tilde{r}_{ijk} = r_{ijk}/h = (i^2 + j^2 + k^2)^{1/2}, \quad (3.10)$$

and the upper (lower) sign is used for  $i > 0$  ( $i < 0$ ). The derivative of  $g$  appearing in (3.9) is to be evaluated at  $t = t_{n+1}$ ,  $x = ih$ ,  $y = jh$ , and  $z = kh$ . The analogous expression for (3.4), using centered differences in  $t$  and one-sided differences in  $x$ , may be written as

$$\begin{aligned} & \left[ 1 + \frac{3\rho\tilde{r}_{ijk}}{2|i|} + \frac{1}{2} \rho\tilde{r}_{ijk} \left( \frac{1}{i^2} + \frac{1}{\tilde{r}_{ijk}^2} \right) \right] \phi_{ijk}^{n+1} \\ &= \left[ 2 \left( 1 - \frac{\rho^2 \tilde{r}_{ijk}^2}{i^2} \right) - \frac{3\rho^2}{|i|} - \rho^2 \left( \frac{1}{k^2} - \frac{1}{\tilde{r}_{ijk}^2} \right) \right] \phi_{ijk}^n \\ & - \left[ 1 - \frac{3\rho\tilde{r}_{ijk}}{2|i|} - \frac{1}{2} \rho\tilde{r}_{ijk} \left( \frac{1}{i^2} + \frac{1}{\tilde{r}_{ijk}^2} \right) \right] \phi_{ijk}^{n-1} \\ & + \frac{\rho\tilde{r}_{ijk}}{|i|} \left[ 2 \left( \phi_{i\mp 1,jk}^{n+1} - \phi_{i\mp 1,jk}^{n-1} \right) - \frac{1}{2} \left( \phi_{i\mp 2,jk}^{n+1} - \phi_{i\mp 2,jk}^{n-1} \right) \right] \\ & + \frac{\rho^2}{|i|} \left[ \left( 4 + \frac{5\tilde{r}_{ijk}^2}{|i|} \right) \phi_{i\mp 1,jk}^n - \left( 1 + \frac{4\tilde{r}_{ijk}^2}{|i|} \right) \phi_{i\mp 2,jk}^n \right. \\ & \left. + \frac{\tilde{r}_{ijk}^2}{|i|} \phi_{i\mp 3,jk}^n \right] + \frac{\rho\tilde{r}_{ijk} \Delta t}{i^2} \tilde{\partial}_x^2 g, \quad (3.11) \end{aligned}$$

where the derivative of  $g$  is evaluated at  $t = t_n$ ,  $x = ih$ ,  $y = jh$ , and  $z = kh$ .

Since the Cartesian boundary points are located in the region covered by the exterior grid (more precisely in the radial interval  $R_m \leq r \leq R_m + h$ ), the derivatives of  $g$  appearing in (3.9) and (3.11) can be calculated by performing finite-differencing on previously evolved characteristic cones  $u = u_m$ ,  $m \leq n + 1$  (see Fig. 6). Let us consider initially the evaluation of  $\tilde{\partial}_x^l g$  ( $l = 1, 2$ ) at a

Cartesian boundary point  $(x_i, y_j, z_k)$  for a retarded time level  $u = u_m$  of the characteristic evolution. A suitable computational cell around  $(x_i, y_j, z_k)$  consists of the grid points

$$(\xi_\alpha, \theta_\beta, \varphi_\beta), \quad \bar{\alpha} - 2 \leq \alpha \leq \bar{\alpha} + 2, \quad \beta \in J. \quad (3.12)$$

where  $\bar{\alpha} \geq 2$  is chosen so that the cell is as centered as possible in the radial direction and

$$(\theta_\beta, \varphi_\beta), \quad \beta \in J \quad (3.13)$$

are the  $N_g$  nearest angular neighbors of  $(x_i, y_j, z_k)$  in the chosen angular discretization. Using the multiquadric technique described in Appendix B, we can then generate finite-difference formulas of the form

$$\tilde{\partial}_x^l g(x_i, y_j, z_k, u_m) = (\Delta \xi)^{-l} \sum_{\alpha=\bar{\alpha}-2}^{\bar{\alpha}+2} \sum_{\beta \in J} c_{\alpha\beta}^{(l)} g_{\alpha\beta}^m, \quad (3.14)$$

where the coefficients  $c_{\alpha\beta}^{(l)}$  are bounded as  $\Delta \xi, \Delta \rightarrow 0$  with  $\Delta/\Delta \xi = \text{const}$ . Note that, although a different set of coefficients is needed at each Cartesian boundary point (since each such point has a distinct neighborhood in the characteristic grid), the same coefficients may be used for all values of  $m$  (because each time level of the characteristic evolution is discretized in exactly the same way). For consistency with the order of accuracy of (3.9) and (3.11), the finite-difference formulas (3.14) are required to have at least second-order accuracy in  $(\Delta, \Delta \xi)$ . As discussed in Appendix B, this accuracy can always be attained provided that  $N_g$  is large enough and the shape parameter  $s = s_g$  involved in the generation of the multiquadric approximations (3.14) is chosen so that  $sg/\Delta \xi = \text{const}$ . as  $\Delta \xi, \Delta \rightarrow 0$  with  $\Delta/\Delta \xi = \text{const}$ . We suggest that  $s_g$  be chosen so that the ratio  $s_g/\min(h_{\text{rad}}, h_{\text{ang}})$  is in the range 2–8, where  $h_{\text{rad}} \simeq R_m^2 \Delta \xi$  and  $h_{\text{ang}} \simeq R_m \Delta$  are the characteristic grid spacings in the radial and angular directions at  $r = R_m$ .

The last step in the approximation of the derivatives of  $g$  appearing in (3.9) and (3.11) involves a quadratic interpolation in  $u$  using derivative values computed by applying (3.14) at three retarded time levels of the characteristic evolution. In (3.9) the value of  $\tilde{\partial}_x g$  at  $(x_i, y_j, z_k)$  is required at the Cauchy time level  $t = t_{n+1}$ , which corresponds to the retarded time

$$u_{ijk}^{n+1} = (n+1)\Delta t - r_{ijk} \leq (n+1)\Delta t - R_m = u_{n+1}.$$

We may then choose  $m \leq n$  such that

$$u_{m-1} < u_{ijk}^{n+1} \leq u_{m+1} \quad (3.15)$$

and obtain the desired value of  $\tilde{\partial}_x g$  by applying (3.14) at the previously evolved time levels  $u = u_{m-1}, u_m, u_{m+1}$  and performing a quadratic interpolation in  $u$ . A completely analogous treatment can be used in the computation of the term  $\tilde{\partial}_x^2 g$  in (3.11). We may also note that, in the initial iterations of the evolution, the values of  $m-1, m$ , or  $m+1$  in (3.15) may sometimes be negative (see Fig. 6), so that the corresponding characteristic cones have not been evolved by the characteristic algorithm. When the initial data and the forcing term satisfy the simplifying assumptions stated at the beginning of this subsection, it is easy to see that the scalar field vanishes in the region  $u \leq \Delta t - R_m, v \geq R_m - \Delta t$ ; then, since (3.15) implies that  $u_{m-1} \geq u_{ijk}^{n+1} - 2\Delta t$ , it follows that the advanced time coordinate of the point with coordinates  $(x_i, y_j, z_k, u_{m-1})$  satisfies the condition

$$\begin{aligned} v &= u_{m-1} + 2r_{ijk} \geq u_{ijk}^{n+1} - 2\Delta t + 2r_{ijk} \\ &= (n-1)\Delta t + r_{ijk} \geq R_m \quad (n \geq 1). \end{aligned}$$

Therefore, whenever  $m-1, m$ , or  $m+1$  happens to be negative in (3.15), the corresponding values of  $\tilde{\partial}_x g$  are zero. (The same result is valid in the analogous scheme for the evaluation of  $\tilde{\partial}_x^2 g$ .) General initial data, which may include incoming waves crossing the hypersurface  $u = -R_m$  for  $r \geq R_m$ , would require a more elaborate initialization procedure, which will not be discussed here.

The use of the above scheme for the evaluation of  $\tilde{\partial}_x^l g$  clearly requires the temporary storage of field values on the exterior grid for a certain number of previously evolved characteristic cones. Since the Cartesian boundary points are restricted to the radial interval  $R_m \leq r < R_m + h$ , it is only necessary to store enough radial layers to cover this interval. If the 5-point radial stencils defined by (3.12) are used with the maximum possible centering, then it can be shown that one must store the layers  $\xi = \xi_\alpha, 0 \leq \alpha \leq \alpha_0$ , where

$$\begin{aligned} \alpha_0 &= \max \left\{ 4, \left[ \frac{1}{\Delta \xi} \left( \frac{1}{R_m} - \frac{1}{R_m + h} \right) \right] + 3 \right\} \\ &= \max \{ 4, [N_\xi/(N+1)] + 3 \}, \end{aligned}$$

where the square brackets denote the integer part. Thus, if the interior and exterior grids are refined by the same factor, the number of radial layers to be stored does not change. With reference to Fig. 6, it may be seen that at the  $n$ th iteration of the algorithm it is necessary to store the innermost  $\alpha_0 + 1$  radial layers of the previously evolved characteristic cones

$$u = u_m, \quad n - \alpha_0 \leq m \leq n + 1.$$

where

$$n_0 = [h/\Delta t] + l$$

and  $l$  is the order of the generalized Sommerfeld condition being employed (1 or 2). As before, the number of time levels to be stored does not change when the discretization is refined keeping  $\rho = \Delta t/h$  constant.

*Step 4. Update the boundary values for the characteristic evolution.* Since the field values at the interior and boundary points of the Cartesian grid have now been computed at time  $t = t_{n+1}$ , new boundary values for the characteristic evolution (at  $r = R_m - \Delta t$ ) may be obtained by three-dimensional interpolation on the Cartesian grid. For this purpose, multiquadric techniques are again convenient, since the boundary set  $\mathcal{B}$  has a somewhat complicated structure. Given a boundary point

$$x_\beta = (R_m - \Delta t) \sin \theta_\beta \cos \varphi_\beta$$

$$y_\beta = (R_m - \Delta t) \sin \theta_\beta \sin \varphi_\beta$$

$$z_\beta = (R_m - \Delta t) \cos \theta_\beta$$

of the characteristic grid,  $\mathcal{N} \subset \mathcal{I} \cup \mathcal{B}$  be the set containing its  $N_B$  nearest neighbors in the Cartesian grid. The multiquadric technique of Appendix B can then be used to approximate  $\tilde{g}_\beta^{n+1}$  as a linear combination of field values  $\phi_{ijk}^{n+1}$  at the grid points belonging to  $\mathcal{N}$ . Interpolation formulas with various orders of accuracy may thus be generated, provided that the shape parameter  $s = s_B$  involved in the multiquadric approximations be chosen so that  $s_B/h = \text{const.}$  as  $h \rightarrow 0$  (we suggest that this ratio be fixed at some value in the range 2–8). In the present algorithm, we require that the boundary interpolations be at least second-order accurate.

#### IV. NUMERICAL RESULTS

This section presents a set of numerical experiments which have been designed to yield information on the following aspects of the Cauchy-characteristic algorithms introduced in the previous sections:

(a) *Stability* The complexity of the three-dimensional matching algorithms makes it virtually impossible to study their stability using normal mode analysis or matrix methods [41] for realistically large grids. Therefore, the numerical study to be presented here is limited to long-term integrations for particular cases of the algorithms.

(b) *Convergence* The experiments involve linear and nonlinear situations with grids of several resolutions. The Richardson extrapolation technique [42] is used to accelerate the convergence of the numerical solutions.

(c) *Comparison with local radiation conditions.* If the terms involving derivatives of  $g$  are neglected in (3.3) and (3.4), we obtain local radiation conditions of the kind usually employed with Cauchy evolutions. These conditions are adapted to purely outgoing spherical waves. The experiments include comparisons between the interior solutions obtained with the matching algorithms and with the above “truncated” conditions. In the remainder of this section, we will denote the matching algorithms with boundary conditions (3.3) and (3.4) by  $C_1$  and  $C_2$ , respectively, and their “truncated” versions by  $S_1$  and  $S_2$ . The matching algorithm of Section II.B will be denoted by I.

(d) *Comparison with nonlocal radiation conditions.* To our knowledge, the only available implementation of time-dependent exact nonlocal boundary conditions for the linear wave equation in three dimensions is due to de Moerloose and de Zutter [14]. This boundary condition is based on an explicit implementation of the Kirchhoff integral formula [43] on a cubic region  $|x|, |y|, |z| \leq R_m = Nh$ , which is discretized in Cartesian coordinates. The Kirchhoff formula is used to express the value of the field at a boundary point of the above cube as a surface integral involving past field values and derivatives over the boundary of the smaller cube described by  $|x|, |y|, |z| \leq R_m - \frac{2}{3}h$ . The algorithm requires that at the  $n$ th time step we store the field values

$$\begin{aligned} \phi_{\pm(N-1),i,j}^m, \quad \phi_{\pm(N-2),i,j}^m, \quad \phi_{i\pm(N-1),j}^m, \quad \phi_{i\pm(N-2),j}^m, \\ \phi_{i,j,\pm(N-1)}^m, \quad \phi_{i,j,\pm(N-2)}^m, \end{aligned}$$

for  $|i|, |j| \leq N - 2$  and  $m = n, n - 1, \dots, n - N_{\text{past}}$ , where

$$N_{\text{past}} = [2\sqrt{3}R_m/\Delta t] = [2\sqrt{3}N/\rho]$$

and  $\rho = \Delta t/h$ . The storage of these past field values requires substantially more memory than the storage of the interior grid values: for a three-level scheme, the ratio between the two memory requirements is about  $12(2N)^2 N_{\text{past}} / 3(2N)^3 = 4\sqrt{3}/\rho$ ; for our interior scheme, which is stable for  $\rho \leq 3^{-1/2}$ , this factor is at least 12. In contrast, for the parameter values used to obtain the results of this paper, the analogous factor for the matching algorithms would be of order unity. Furthermore, due to nonlocality, the number of arithmetic operations per time step grows as  $N^4$ , as compared to  $N^3$  for the matching algorithms (the matching procedure itself makes only a  $O(N^2)$  contribution to the total number of operations).

We have independently implemented the de Moerloose-de Zutter algorithm (henceforth referred to as algorithm K) following the description given in [14]. The code runs on a Cray C90 at about 330 Mflops, a speed similar to that of our matching codes (180–350 Mflops). However,

the CPU time per time step required by the de Moerloose–de Zutter algorithm was about 500 times that required by the matching codes. This larger CPU time is clearly not due to inefficient coding; there are also no free parameters in the de Moerloose–de Zutter algorithm which could be adjusted to make it more efficient. Our results on the performance of algorithm K serve also to supplement those given in [14], where its supposed convergence to the exact solution of the linear wave equation was not tested.

(e) *Sensitivity of the numerical solutions to the position of the matching interface.* For each fixed value of  $R_m$ , the numerical solutions obtained with the matching algorithms should converge to the exact solution of the (linear or nonlinear) initial-value problem being considered. In general, the solutions obtained using linear local ABC's (such as  $S_1$  and  $S_2$ ) should converge to a limit which depends on the chosen value of  $R_m$  (this limit should approach the exact solution when  $R_m \rightarrow \infty$ ). An exact (in the linear sense) ABC such as K should converge to the exact solution in linear problems, and behave as a linear local ABC in strongly nonlinear problems. Therefore, in such situations we expect the numerical results obtained with algorithms  $C_1$ ,  $C_2$ , and I to be significantly less sensitive to the choice of  $R_m$  than those obtained with  $S_1$ ,  $S_2$ , and K.

(f) *Sensitivity of the numerical solutions to the order of the boundary conditions.* The solutions obtained with algorithms  $C_1$  and  $C_2$  should both converge to the exact solution of the initial-value problem; on the other hand, there is no reason to expect that the solutions using  $S_1$  and  $S_2$  will converge to a common limit, except when  $R_m \rightarrow \infty$ . Therefore, we expect the numerical results obtained with  $C_1$  and  $C_2$  to be more similar to each other than those obtained with  $S_1$  and  $S_2$ .

### A. Stability

The stability properties of the matching algorithms I,  $C_1$ , and  $C_2$  have been investigated by performing long-term integrations of the linear wave equation with initial data which excite mainly the shortest waves resolved by the computational grid, such as random or alternating-sign initial data. In this kind of experiment, stable algorithms exhibit an exponential decay of the maximum norm  $\|\phi\|_\infty$ , while unstable algorithms feature exponential growth. A typical test integration was carried out for up to  $O(10^5)$  time steps (corresponding to a time interval  $0 \leq t \leq O(10^3 R_m)$ ), which were generally sufficient to clearly distinguish between stable and unstable cases.

(a) *Algorithm I.* Among the free parameters  $M$ ,  $N_s$ ,  $N_\eta$ ,  $\rho (= \Delta t/h)$ ,  $K$ , and  $R_m$ , we fixed  $R_m = 1$  and  $M = 22$ , and varied the remaining ones as functions of  $N_s$  and  $N_\eta$ . There is no loss of generality in assuming that  $R_m = 1$ ,

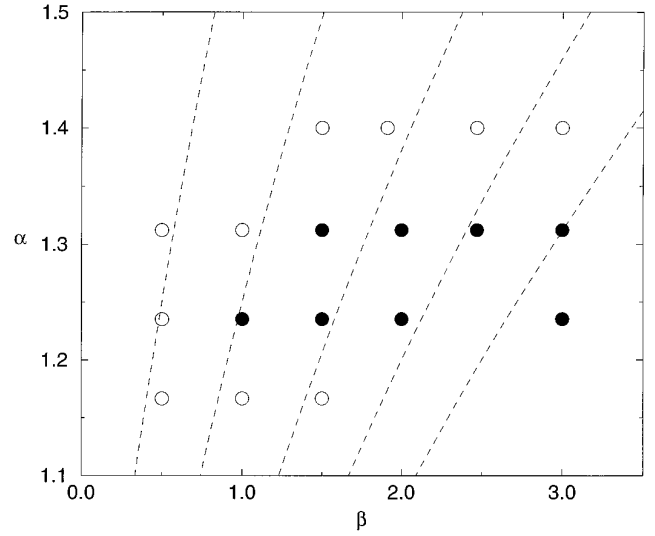


FIGURE 7

since a simple scaling argument shows that the stability properties of the matching algorithm I do not change when  $R_m$  and  $\Delta t$  are scaled by the same factor and  $M$ ,  $N_s$ ,  $N_\eta$ , and  $K$  are kept fixed. (An analogous property holds for the matching algorithms  $C_1$  and  $C_2$ .) The Courant number  $\rho = \Delta t/h$  was chosen as

$$\rho = \frac{1}{2}\rho_{\max}, \quad (4.1)$$

where  $\rho_{\max}$  is the maximum value of  $\rho$  which satisfies the domain of dependence conditions given by (2.11) with  $r = R_m$ ,  $q = p = 1$ ,  $\Delta u = \Delta t$ ;

$$\rho_{\max} = \min\{2\beta, -\beta + (\beta^2 + \frac{4}{9}\alpha^2)^{1/2}\}, \quad (4.2)$$

with

$$\alpha = \frac{R_m \Delta s}{h} = \frac{M-1}{N_s}, \quad \beta = \frac{\Delta r}{h} = \frac{2(M-1)}{N_\eta - 1}, \quad (4.3)$$

where  $\Delta r$  is the difference between the radii of the first two radial (characteristic) grid points. The parameter  $K$  was then chosen according to (2.12).

Figure 7 shows the results of the numerical study in terms of the dimensionless parameters  $\alpha$  and  $\beta$ . The results indicate that there is a stable region around  $\alpha = 1.25$ ,  $\beta = 2$ , but that instabilities occur when either  $\alpha$  is greater than about 1.3 or  $\beta$  is less than about 1.0.

(b) *Algorithms  $C_1$  and  $C_2$ .* Since the algorithms  $C_1$  and  $C_2$  contain many free parameters ( $R_m$ ,  $h$ ,  $\Delta$ ,  $\Delta \xi$ ,  $\Delta t$ ,  $s_g$ ,  $s_L$ ,  $s_B$ ,  $N_g$ ,  $N_L$ ,  $N_B$ ), we have fixed  $R_m$ ,  $h$ ,  $N_g$ ,  $N_L$ , and  $N_B$  and varied the remaining parameters so that the ratios  $\Delta/R_m \Delta \xi$  ( $\approx h_{\text{ang}}/h_{\text{rad}}$ ),  $s_g/R_m \Delta$  ( $\approx s_g/h_{\text{ang}}$ ),  $s_L/\Delta$ , and  $s_B/h$  remained

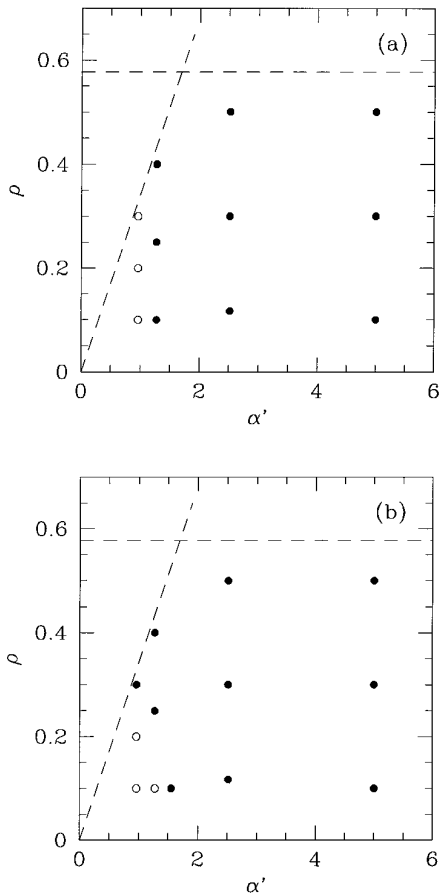


FIGURE 8

constant. We may therefore choose  $\rho = \Delta t/h$  and  $\alpha' = R_m \Delta/h \approx h_{\text{ang}}/h$  as the independent variables in the stability study (the parameter  $\alpha'$  is analogous to the ratio  $\alpha$  employed earlier in this section). The numerical results (Fig. 8) indicate that, under the conditions of the experiment ( $R_m = \frac{182}{17}$ ,  $N = 21$ ,  $h = \frac{26}{51}$ ,  $N_g = 20$ ,  $N_L = 31$ ,  $N_B = 125$ ,  $\Delta/R_m \Delta \xi \approx 2.1$ ,  $s_g/R_m \Delta \approx 3.7$ ,  $s_L/\Delta \approx 14$ ,  $s_B/h = 8$ ), both  $C_1$  and  $C_2$  are stable over most of the region in the  $(\alpha', \rho)$  plane which is determined by the CFL conditions for the Cauchy and characteristic evolutions. Instabilities associated with the boundary updating scheme only appear for sufficiently small values of  $\alpha'$ . However, in many cases that we have examined, decreasing the values of the ratios  $s_B/h$  and  $s_g/R_m \Delta$  led to a reduction in the lower stability limit for  $\alpha'$ , thereby allowing the use of finer exterior grids. For example, the three unstable cases for algorithm  $C_1$  which appear in Fig. 8a can be stabilized by reducing  $s_B/h$  and  $s_g/R_m \Delta$  from 8 to 4 and from 3.7 to 1.8, respectively, while maintaining the remaining parameters unchanged.

We have also carried out experiments which suggest that the stability of either  $C_1$  or  $C_2$  is preserved when the time step  $\Delta t$ , the grid spacings  $h$ ,  $\Delta$ , and  $\Delta \xi$ , and the shape

parameters  $s_g$ ,  $s_L$ , and  $s_B$  are multiplied by a common factor  $0 < \lambda < 1$  (the remaining parameters  $R_m$ ,  $N_g$ ,  $N_L$ , and  $N_B$  are kept unchanged).

The domain of stability of the algorithms based on generalized Sommerfeld conditions ( $C_1$  and  $C_2$ ) includes most of the combinations of grid spacings and time step which are allowed by the CFL conditions for the Cauchy and characteristic evolution schemes. When these conditions are satisfied, instabilities have been observed only when  $\Delta t/h$ ,  $h_{\text{ang}}/h \approx R_m \Delta/h$ , and  $h_{\text{rad}}/h \approx R_m^2 \Delta \xi/h$  are all relatively small. In such cases, the available numerical evidence suggests that the algorithms may often be stabilized by adjusting the free parameters associated with the multi-quadratic approximations ( $s_g$ ,  $s_L$ ,  $s_B$ ,  $N_g$ ,  $N_L$ ,  $N_B$ ), without having to change either the grid spacings or the time step. Comparing Figs. 7 and 8, it can be seen that the stability conditions for our interpolation-based matching algorithm (I) are somewhat more restrictive than those for algorithms  $C_1$  and  $C_2$ , usually requiring the use of finer angular discretizations.

## B. Grid Parameters

In order to study the dependence of the numerical solutions on the resolution of the computational grids and on the position of the matching interface, we performed experiments with interfaces at two different radii ( $R_m = \frac{182}{17}$  and  $R_m = \frac{234}{17}$ ), using grids of increasing resolution. The duration of the simulations (from  $t = 0$  to  $t = 70$ ) was chosen to allow any spuriously reflected waves to cross the interior computational domain several times.

In the tests involving algorithms  $C_1$  and  $C_2$ , for each value of  $R_m$ , we constructed a sequence of discretizations of spacetime such that the parameters  $h$ ,  $\Delta t$ ,  $\Delta$ , and  $\Delta \xi$  vary linearly with an arbitrary parameter  $\lambda$ ; the sequences with  $R_m = \frac{182}{17}$  and  $R_m = \frac{234}{17}$  are denoted by  $N_\lambda$  and  $F_\lambda$  (“near” and “far” boundaries), respectively (Table I). According to the general methodology of Appendix B, the numbers of points in the stencils of the multi-quadratic-based approximations (determined by the parameters  $N_L$ ,  $N_g$ , and  $N_B$ ) are kept fixed as the grids are refined, while the corresponding shape parameters ( $s_L$ ,  $s_g$ , and  $s_B$ ) are taken to be proportional to  $\lambda$ . In all experiments, we choose  $N_L = 31$ ,  $N_g = 20$ , and  $N_B = 125$ . Since all approximations involved in the matching algorithms are at least second-order accurate, we expect that for each sequence the error of the numerical solutions will be  $O(\lambda^2)$  as  $\lambda \rightarrow 0$ . The “truncated” algorithms  $S_1$  and  $S_2$  should also exhibit second-order convergence (to limits which are generally different from the exact solution). Using long-term integrations, we have verified that the algorithms  $C_1$ ,  $C_2$ ,  $S_1$ , and  $S_2$  are stable for all the discretizations shown in Table I.

The parameter values in Table I have been chosen so that the numerical results obtained with different discretiz-



**TABLE I**

Parameters of the Discretizations Employed in the Numerical Experiments with Algorithms  $C_1$ ,  $C_2$ ,  $S_1$ , and  $S_2$

Discretization	$R_m$	$N$	$h$	$\Delta t$	$N_\xi$	$\Delta \xi$	$N_{\text{ang}}$	$\Delta$	$s_B$	$s_g$	$s_L$
$N_{4/3}$	$\frac{182}{17}$	21	$\frac{26}{51}$	$\frac{91}{1530}$	17	$\frac{1}{182}$	860	0.1198	4.1	4.7	1.67
$N_1$	$\frac{182}{17}$	28	$\frac{13}{34}$	$\frac{91}{2040}$	22	$\frac{17}{4004}$	1528	0.0913	3.1	3.5	1.25
$N_{4/5}$	$\frac{182}{17}$	35	$\frac{26}{85}$	$\frac{91}{2550}$	28	$\frac{17}{5096}$	2388	0.0738	2.4	2.8	1.00
$N_{2/3}$	$\frac{182}{17}$	42	$\frac{13}{51}$	$\frac{91}{3060}$	34	$\frac{1}{364}$	3439	0.0607	2.0	2.3	0.83
$N_{1/2}$	$\frac{182}{17}$	56	$\frac{13}{68}$	$\frac{91}{4080}$	45	$\frac{17}{8190}$	6112	0.0460	1.5	1.8	0.63
$F_{4/3}$	$\frac{234}{17}$	27	$\frac{26}{51}$	$\frac{13}{255}$	16	$\frac{17}{3744}$	860	0.1198	4.1	5.8	1.67
$F_1$	$\frac{234}{17}$	36	$\frac{13}{34}$	$\frac{13}{340}$	21	$\frac{17}{4914}$	1528	0.0913	3.1	4.4	1.25
$F_{4/5}$	$\frac{234}{17}$	45	$\frac{26}{85}$	$\frac{13}{425}$	26	$\frac{17}{6084}$	2388	0.0738	2.4	3.5	1.00
$F_{2/3}$	$\frac{234}{17}$	54	$\frac{13}{51}$	$\frac{13}{510}$	32	$\frac{17}{7488}$	3439	0.0607	2.0	2.9	0.83

ations can be directly compared at certain points in space-time. Thus, all interior solutions can be compared for

$$t = \frac{364}{85}n, \quad n = 0, 1, 2, \dots \quad (4.4)$$

at the grid points

$$x = \frac{26}{17}i, \quad y = \frac{26}{17}j, \quad z = \frac{26}{17}k, \quad (4.5)$$

where  $i, j, k$  are integers satisfying

$$(i^2 + j^2 + k^2)^{1/2} \leq 6. \quad (4.6)$$

It is also possible to make certain comparisons between exterior solutions, since the discretizations in Table I contain families of common characteristic cones. For example, the cones of the form

$$u = \frac{1092n - 2002}{255}, \quad (4.7)$$

$$u = \frac{364n - 910}{85}, \quad (4.8)$$

$n = 0, 1, 2, \dots$ , are common to the discretizations  $N_\lambda$  and  $F_\lambda$ , respectively.

Similarly, in the experiments with matching algorithm I, we employed spacetime discretizations  $N'_\lambda$  and  $F'_\lambda$  (Table II) which resemble  $N_\lambda$  and  $F_\lambda$  very closely. The main differ-

ence between the two sets of discretizations lies in their angular resolution, which is significantly higher for  $N'_\lambda$  and  $F'_\lambda$  in order to ensure the stability of algorithm I. In all experiments, the parameter  $K$  is chosen according to (2.12).

The interior solutions obtained with the discretizations shown in Table II can be directly compared for the time levels (4.4) at the grid points

$$x = \frac{26}{17}(i - \frac{1}{2}), \quad y = \frac{26}{17}(j - \frac{1}{2}), \quad z = \frac{26}{17}(k - \frac{1}{2}), \quad (4.9)$$

where  $i, j$ , and  $k$  are integers such that

$$[(i - \frac{1}{2})^2 + (j - \frac{1}{2})^2 + (k - \frac{1}{2})^2]^{1/2} \leq \frac{13}{2}. \quad (4.10)$$

The retarded time levels (4.7) and (4.8) are common to the discretizations  $N'_\lambda$  and  $F'_\lambda$ , respectively, and can again be used in direct comparisons between the exterior solutions.

For the tests involving algorithm K, we use the discretizations  $N''_\lambda$  and  $F''_\lambda$ , whose parameters are shown in Table III. These are identical to the corresponding parameters in Table I, with the difference that the time step is four times larger. This larger time step was needed to limit the total computer time required by the experiments (see item (d) at the beginning of this section). Also, due to computa-

**TABLE II**

Parameters of the Discretizations Employed in the Numerical Experiments with Algorithm I

Discretization	$R_m$	$M$	$h$	$\Delta t$	$N_\eta$	$\Delta \eta$	$N_s$	$N_{\text{ang}}$	$\Delta s$
$N'_{4/3}$	$\frac{182}{17}$	22	$\frac{26}{51}$	$\frac{91}{1530}$	18	$\frac{1}{36}$	24	4802	$\frac{1}{24}$
$N'_{4/5}$	$\frac{182}{17}$	36	$\frac{26}{85}$	$\frac{91}{2550}$	30	$\frac{1}{60}$	40	13122	$\frac{1}{40}$
$N'_{4/7}$	$\frac{182}{17}$	50	$\frac{26}{119}$	$\frac{13}{510}$	42	$\frac{1}{84}$	56	25538	$\frac{1}{56}$
$F'_{4/3}$	$\frac{234}{17}$	28	$\frac{26}{51}$	$\frac{13}{255}$	18	$\frac{1}{36}$	24	4802	$\frac{1}{24}$
$F'_{4/5}$	$\frac{234}{17}$	46	$\frac{26}{85}$	$\frac{13}{425}$	30	$\frac{1}{60}$	40	13122	$\frac{1}{40}$

Note. In this table,  $N_{\text{ang}} = 2(2N_s + 1)^2$  represents the total number of angular grid points on the stereographic discretization of the unit sphere.

**TABLE III**

Parameters of the Discretizations Employed in the Numerical Experiments with Algorithm K

Discretization	$R_m$	$N$	$h$	$\Delta t$
$N_{4/3}''$	$\frac{182}{17}$	21	$\frac{26}{51}$	$\frac{182}{765}$
$N_1''$	$\frac{182}{17}$	28	$\frac{13}{34}$	$\frac{91}{510}$
$F_2''$	$\frac{234}{17}$	18	$\frac{13}{17}$	$\frac{26}{85}$
$F_{4/3}''$	$\frac{234}{17}$	27	$\frac{26}{51}$	$\frac{52}{255}$

tional resource limitations we have restricted the experiments with algorithm  $K$  to relatively coarse grids ( $N \leq 28$ ). Finally, it should be kept in mind that, although the grid spacing  $h$  and the value of  $R_m$  are the same for corresponding discretizations in Tables I and III, the computational boundary is a cube of side  $2R_m$  for algorithm  $K$  and a sphere of diameter  $2R_m$  for all other algorithms.

In the description of the numerical tests, we use a special notation to distinguish between the solutions obtained with the various algorithms and discretizations. Thus, for example,  $\phi_\lambda^{C_2N}$  denotes the solution obtained with algorithm  $C_2$  using discretization  $N_\lambda$ , and  $\phi_\lambda^{IF'}$  denotes the solution obtained with algorithm  $I$  and discretization  $F'_\lambda$ . We use the Richardson extrapolation technique to estimate the limits to which the different numerical solutions are converging as the grids are refined. The extrapolated solutions are also identified by a special notation. For example,  $\phi_{2/3, 1/2}^{C_2N}$  denotes the result of Richardson extrapolation applied to  $\phi_{2/3}^{C_2N}$  and  $\phi_{1/2}^{C_2N}$ .

### C. Experiments with the Linear Wave Equation

As a first test of the matching algorithms based on generalized Sommerfeld conditions, we consider the numerical solution of initial-value problems for the linear wave equation driven by an external source  $S(x, y, z, t)$ . This is a convenient test because the exact solution is given in closed form by the Kirchhoff integral [43]

$$\phi(x, y, z, t) = \frac{1}{4\pi} \iiint_{r' \leq t} \frac{S(x', y', z', t - r')}{r'} dx' dy' dz'. \quad (4.11)$$

where  $r' = [(x - x')^2 + (y - y')^2 + (z - z')^2]^{1/2}$  (the initial data are  $\phi = \partial_t \phi = 0$  at  $t = 0$ ). We will first construct a simple spherical source model for which the above integral can be evaluated analytically and then test the algorithms  $C_1$ ,  $C_2$ ,  $S_1$ ,  $S_2$ ,  $I$ , and  $K$  with a superposition of the resulting spherically symmetric solutions with centers at various positions inside the Cartesian grid.

For spherically symmetric sources,  $S = S(r, t)$ , it can be shown that (4.11) reduces to

$$\phi(r, t) = \frac{1}{2r} \int_0^t dr' \int_{|r-r'|}^{r+r'} dr'' r'' S(r'', t - r'). \quad (4.12)$$

As our source model, we take the time-harmonic, finite-radius forcing distribution

$$S(r, t) = S_0 Q(r) \sin \omega t, \quad (4.13)$$

$$Q(r) = \begin{cases} \frac{1}{2}[1 + \cos(\pi r/r_0)], & r \leq r_0 \\ 0 & r > r_0. \end{cases} \quad (4.14)$$

Inserting the above forcing function in (4.12), one obtains, after a long but straightforward calculation, the desired exact solution of the forced wave equation (the result is presented in Appendix C).

In our numerical experiments, we employed a superposition of spherical sources with the above structure, whose parameter values are given in Table IV. The forced linear wave equation with homogeneous initial conditions was then solved using algorithms  $C_1$ ,  $C_2$ ,  $S_1$ ,  $S_2$ ,  $I$ , and  $K$  and the discretizations shown in Tables I, II, and III. The results of the tests (Figs. 9 and 10) confirm the second-order convergence of the matching algorithms  $C_1$ ,  $C_2$ , and  $I$ , and clearly display the limitations of the local boundary conditions employed by algorithms  $S_1$  and  $S_2$ . The solutions obtained with these two schemes converge to limits which depend both on the order of the boundary conditions (Figs. 9a and 9c) and on the radius of the Cartesian grid (not shown). The matching schemes, on the other hand, produce solutions whose errors systematically decrease with increasing resolution (Figs. 9b, 9d, 9f, and 10). The results for algorithm  $K$  (Fig. 9e) suggest that it is also converging to the exact solution at a second-order rate, although more resolution would be needed to see this more clearly. The higher error level obtained for  $K$  in comparison with the matching algorithms seems to be due to the lower resolution used with the nonlocal method. The extrapolated solution from algorithm  $K$  outperforms all solutions from  $S_1$  and  $S_2$ , even though it is obtained from relatively low resolution solutions.

**TABLE IV**

Parameters of the Spherically Symmetric Solutions Used in the Experiment with the Linear Wave Equation

Source	$x_0$	$y_0$	$z_0$	$r_0$	$\omega$	$S_0$
1	0.71	0.71	0.00	3	0.6	1.0
2	1.00	-2.00	-2.00	2	0.5	-0.5
3	3.00	1.00	2.45	2	0.3	0.8
4	-3.00	-2.00	2.30	3	0.8	-0.3

*Note.* Here  $x_0$ ,  $y_0$ , and  $z_0$  denote the coordinates of the centers of symmetry of each solution.

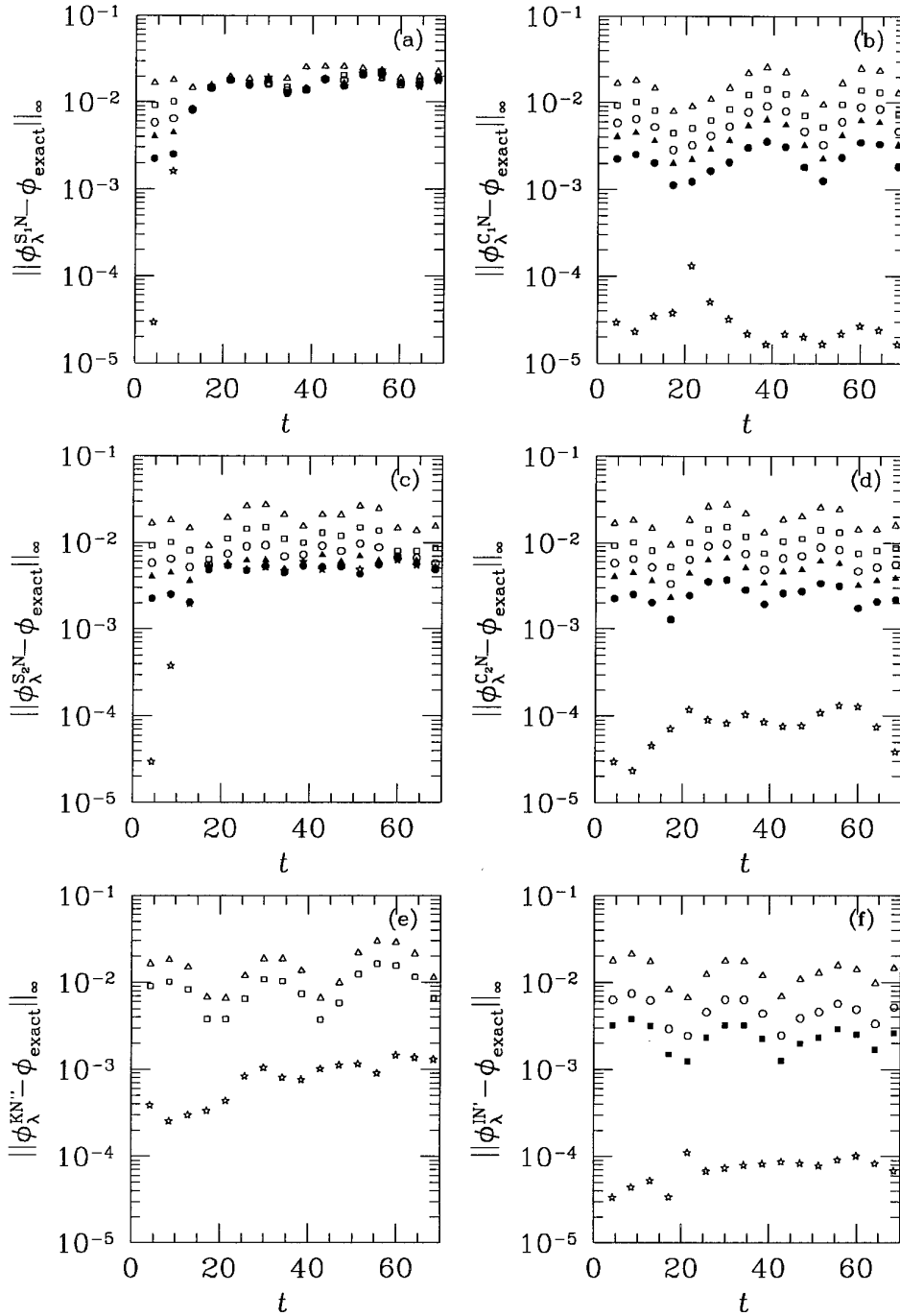


FIGURE 9

#### D. Experiments with a Nonlinear Wave Equation

In this set of experiments, two initial-value problems involving the forced nonlinear wave equation

$$\partial_t \phi = \nabla^2 \phi - 4\phi^3 + S(x, y, z, t) \quad (4.15)$$

are solved using the schemes  $C_1$ ,  $C_2$ ,  $S_1$ ,  $S_2$ , I, and K.

The two problems differ only in the choice of the forcing function  $S$ ; in both cases, the initial conditions are  $\phi = \partial_t \phi = 0$  at  $t = 0$ .

*Experiment 1 (spherical symmetry).* If the forcing  $S$  has spherical symmetry about the origin  $r = 0$ , the solution of the initial-value problem will also be spherically symmetric. However, due to the presence of nonlinear effects (back-

scattering), the Sommerfeld radiation condition (as well as the boundary conditions used in schemes  $S_1$  and  $S_2$ , which are also adapted to spherical outgoing waves) will not be exactly satisfied at the boundary of the interior computational domain. The linear assumptions of the non-local algorithm  $K$  will also be violated. The forcing employed in this experiment is the finite-radius harmonic source defined by (4.13) and (4.14) with  $S_0 = 0.2$ ,  $\omega = 0.3$ ,  $r_0 = 7$ .

Although the exact solution of this initial-value problem is not known, very accurate approximations to the solution may be obtained by performing high-resolution runs of a one-dimensional finite-difference code which solves the spherically symmetric version of (4.15). In such runs, the outer computational boundary must be placed at a sufficiently large radius that the emitted wavefront will reach the boundary only after the end of the time integration. In this case, the one-dimensional numerical solutions are unaffected by boundaries, and should converge to the exact solution of the initial-value problem. Our “reference solu-

tion”  $\phi_{1-D}$  was obtained by applying Richardson extrapolation to two integrations having radial grid spacings  $h = 8 \times 10^{-3}$  and  $4 \times 10^{-3}$ . The integrations extended from  $t = 0$  to  $t = 70$  (corresponding to roughly three complete oscillations of the source), and the outer boundary was situated at  $R_m = 100$ ; the ratio  $\rho = \Delta t/h$  was fixed at 0.328.

We have also solved this problem with a one-dimensional code which implements the spherically symmetric version of our matching algorithm  $C_1$  using similar interior resolutions ( $h = 7.353 \times 10^{-3}$ ,  $3.676 \times 10^{-3}$ ,  $\rho = 0.379$ ), but with computational interfaces located at much smaller radii (we used  $R_m = 182/17$  and  $R_m = 234/17$ , which are the same used in the three-dimensional discretizations  $N_\lambda$  and  $F_\lambda$ , respectively). The number of radial characteristic grid points was chosen as  $N_\xi = 0.687N$  for the runs with  $R_m = 182/17$  and  $N_\xi = 0.534N$  for the runs with  $R_m = 234/17$ , where  $N$  is the number of interior grid points. The boundary condition in this code is a discrete version of (3.1); the derivative  $\tilde{\partial}_r g|_{r=R_m} = -R_m^{-2} \tilde{\partial}_\xi g|_{\xi=\xi_0}$  appearing in this boundary condition is evaluated by standard one-sided

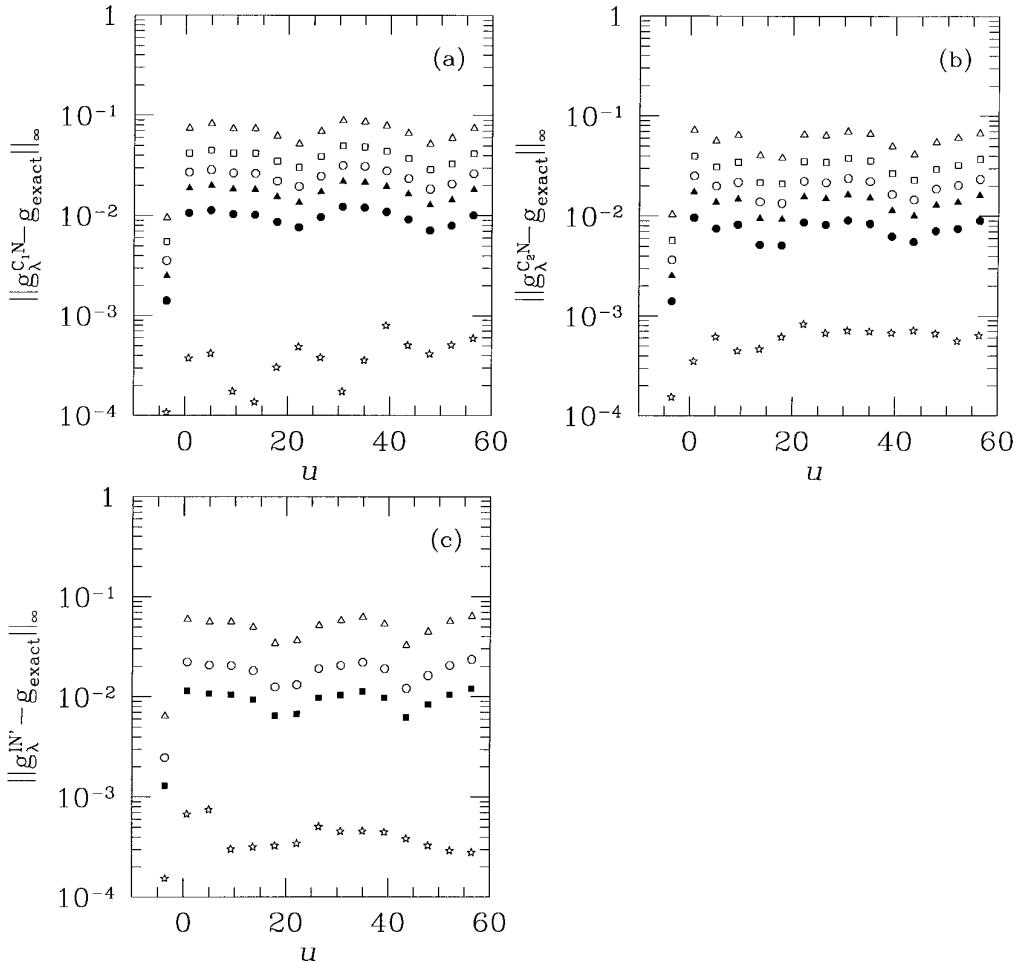


FIGURE 10

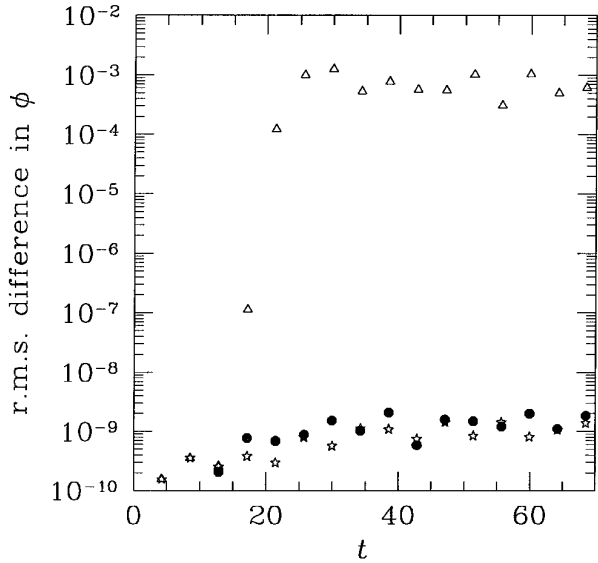


FIGURE 11

differences on the characteristic grid. The updating of the characteristic grid point at  $r = R_m - \Delta t$  (point  $B$  in Fig. 6) may be performed by quadratic interpolation on the interior grid. The interior and exterior evolution algorithms are the same as in Sections II.A and III.B, respectively, with the simplification that all angular derivative terms vanish. The extrapolated matching solution  $\phi_{1-D}^{C_1F}$  (obtained from the solutions with  $R_m = 234/17$ ) coincides with the previously obtained “reference solution” with a relative accuracy  $\|\phi_{1-D}^{C_1F} - \phi_{1-D}\|_2 / \|\phi_{1-D}\|_2 < 2.2 \times 10^{-8}$  (Fig. 11). Furthermore, the extrapolated matching solution  $\phi_{1-D}^{C_1F}$  (obtained from the solutions with  $R_m = 234/17$ ) coincides with  $\phi_{1-D}^{C_1F}$  with a relative accuracy  $\|\phi_{1-D}^{C_1F} - \phi_{1-D}^{C_1N}\|_2 / \|\phi_{1-D}\|_2 < 2.3 \times 10^{-8}$  (Fig. 11). The excellent agreement between all three independent one-dimensional solutions indicates that their common relative accuracy is  $O(10^{-8})$ ; it is also strong evidence that the matching solutions converge to the exact solution of this nonlinear initial-value problem. We may also note that, since the error obtained with feasible three-dimensional code runs is much larger than the previous estimate, we can safely consider  $\phi_{1-D}$  as identical to the exact solution when estimating the errors from algorithms  $C_1$ ,  $C_2$ ,  $S_1$ ,  $S_2$ ,  $I$ , and  $K$ .

For comparison, we also show in Fig. 11 an extrapolated high-resolution solution of the same problem using the spherically symmetric version of the local boundary condition  $S_2$  (obtained by setting  $x = r$  in (3.4) and neglecting the right-hand side). As expected, the solutions  $\phi_{1-D}^{S_2F}$  using this boundary condition (with the same values of  $h$ ,  $\rho$ , and  $R_m$  as in  $\phi_{1-D}^{C_1F}$ ) do not converge to the reference solution, and therefore (since  $\|\phi_{1-D}^{S_2F} - \phi_{1-D}\|_2 = O(10^{-3}) \gg \|\phi_{1-D} - \phi_{\text{exact}}\|_2 = O(10^{-9})$ ) do not converge to the exact

solution. The analogous results for the spherically symmetric version of  $S_1$  yield even larger errors. Although we have not included other existing ABC’s in this comparison, it seems very unlikely that these approaches, which do not take the exterior nonlinearity into account, could produce solutions with accuracy comparable to that of the above matching solutions.

The results of our three-dimensional runs (Fig. 12) indicate that, as in the linear case, the matching solutions converge at a second-order rate to the exact solution of the nonlinear initial-value problem. The error levels of the linear boundary algorithms ( $S_1$ ,  $S_2$ , and  $K$ ) are much higher than those obtained with matching, and are essentially independent of grid resolution. This is clearly due to the presence of nonlinearity in the exterior domain. Even though the resolution used with algorithm  $K$  was lower than that used with the other methods, the small decrease in error between the  $N'_{4/3}$  and  $N'_1$  discretizations (Fig. 12e) suggests that no significant improvement would be achieved by further increasing the resolution.

*Experiment 2 (ellipsoidal sources).* This experiment includes both nonlinear and nonspherical effects; the forcing consists of a superposition of two ellipsoidal sources with structure

$$S(x, y, z, t) = S_0 Q(x, y, z) \sin \omega t,$$

$$Q(x, y, z) = \begin{cases} \frac{1}{2}[1 + \cos(\pi q(x, y, z))] & q(x, y, z) \leq 1 \\ 0 & q(x, y, z) > 1, \end{cases}$$

where

$$q(x, y, z) = \left[ \frac{(\Delta x')^2}{A^2} + \frac{(\Delta y')^2}{B^2} + \frac{(\Delta z')^2}{C^2} \right]^{1/2}$$

and

$$\begin{aligned} \Delta x' &= (x - x_0) \cos \beta \cos \alpha + (y - y_0) \sin \beta \cos \alpha \\ &\quad + (z - z_0) \sin \alpha \\ \Delta y' &= (y - y_0) \cos \beta - (x - x_0) \sin \beta \\ \Delta z' &= (z - z_0) \cos \alpha - (x - x_0) \cos \beta \sin \alpha \\ &\quad - (y - y_0) \sin \beta \sin \alpha. \end{aligned}$$

The parameters of the sources are shown in Table V.

Although independent highly accurate approximations to the solution of this initial-value problem are difficult to obtain, it is simple to compare the sensitivity of various schemes to changes in the matching radius and in the order of the radiation boundary conditions. A detailed analysis shows that, for each  $i$ , the matching algorithm  $C_i$  and the linear boundary algorithm  $S_i$  approach their (distinct) lim-

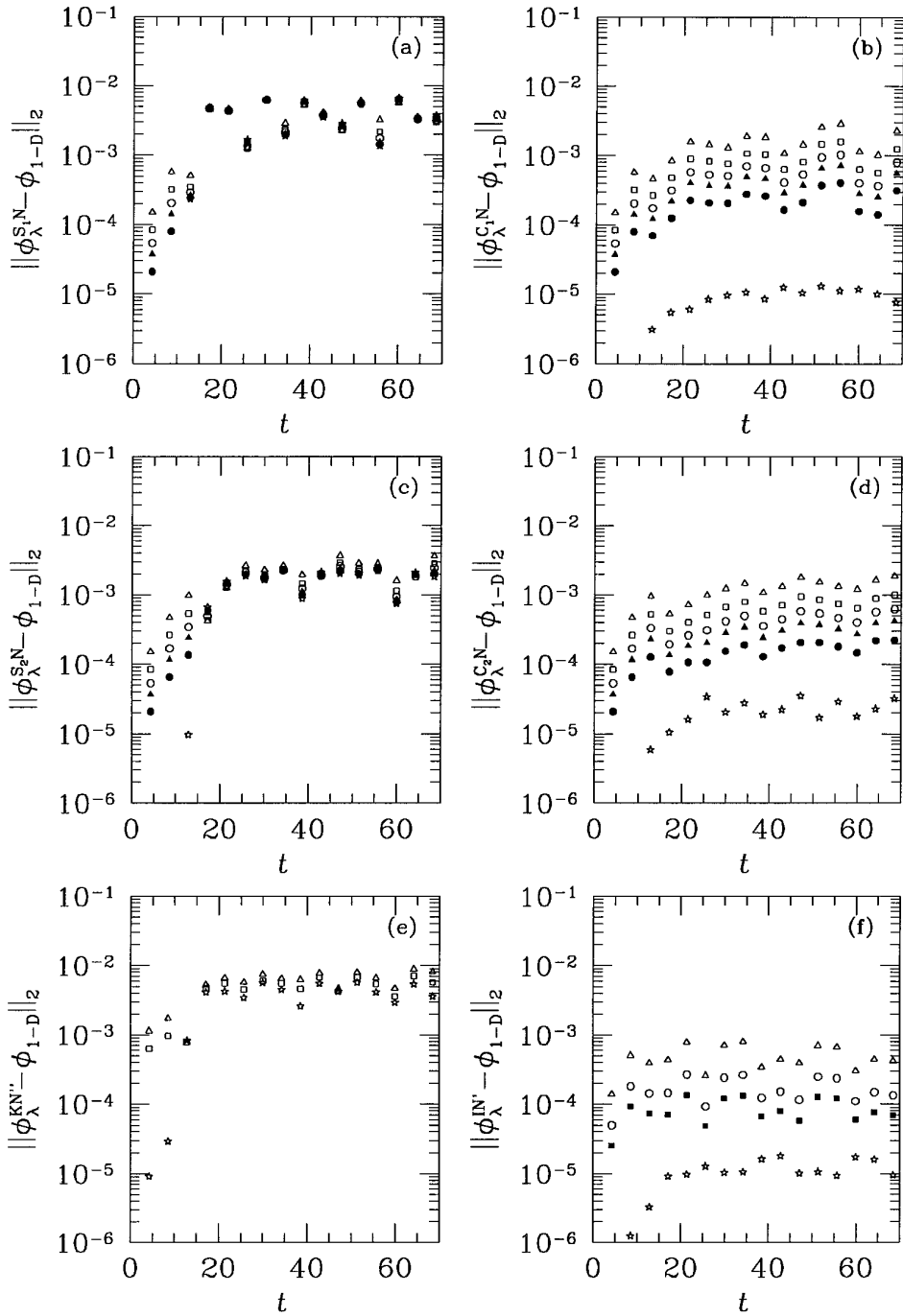


FIGURE 12

its at very similar rates. However, as we would expect from the previous experiments, the results obtained with the schemes  $S_i$  are much more sensitive to changes in  $R_m$  and  $i$  than those obtained with the matching schemes  $C_i$  (Figs. 13 and 14). The solutions using the matching algorithm I are also very insensitive to changes in the matching radius

(Fig. 13). Even though we could not investigate algorithm K at high resolution, for this particular problem its sensitivity seems to be similar to that of  $S_2$  (Fig. 13). Furthermore, a detailed analysis of the numerical results indicates that the sensitivity of the schemes  $C_1$ ,  $C_2$ , and I can always be reduced by increasing the grid resolution, while the

**TABLE V**  
Parameters of the Ellipsoidal Sources Used in Experiment 2

Source	$x_0$	$y_0$	$z_0$	$A$	$B$	$C$	$\alpha$	$\beta$	$\omega$	$S_0$
1	6	1	0	1.5	2.5	1.5	0	0	0.5	1
2	2	-3	0	4.0	2.0	2.0	20	50	0.3	-1

*Note.* The angles  $\alpha$  and  $\beta$  are given in degrees.

sensitivity of the schemes  $S_1$  and  $S_2$  (and probably also K) rapidly becomes independent of resolution. Therefore, it seems very likely that the common limit to which all matching schemes are converging is actually the exact solution of the nonlinear initial-value problem.

## V. CONCLUSIONS

We have presented and tested two alternative formulations of three-dimensional Cauchy-characteristic matching for the scalar wave equation. In one formulation (algorithm I, Section II), the boundary values for the interior and exterior evolutions are obtained by an interpolation scheme at constant time which uses data from both interior and exterior grids. The formulation based on generalized Sommerfeld conditions (algorithms  $C_i$ , Section III) essentially uses the characteristic evolution scheme to correct a boundary condition often employed in Cauchy evolutions. In both algorithms, no special assumption is made about the waves crossing the computational interface  $r = R_m$ ,

other than the smoothness of the scalar field. Nonlinear effects in the exterior computational domain are automatically taken into account by the matching algorithms, provided that the asymptotic behavior of the wave field at radiative infinity is that of a nondispersive outgoing wave.

In our numerical experiments it was found that the various matching methods were all convergent to the exact solution (with a computational interface located at an arbitrary fixed position) in both linear and nonlinear problems. As expected, the nonlocal boundary condition K yielded convergent results only when its assumptions were respected that is, in linear problems. Convergence was not observed for the linear local boundary conditions  $S_1$  and  $S_2$ , whose restrictive assumptions were violated in all of our numerical experiments. For each matching algorithm, a region of parameter space was found in which the algorithm is stable. The stability conditions for our interpolation-based matching algorithm (I) are somewhat more restrictive than those for algorithms  $C_1$  and  $C_2$ , usually requiring the use of finer angular discretizations.

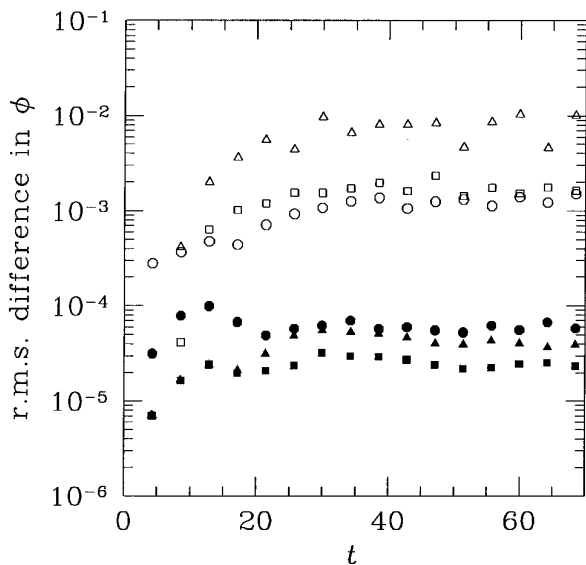


**FIGURE 13**

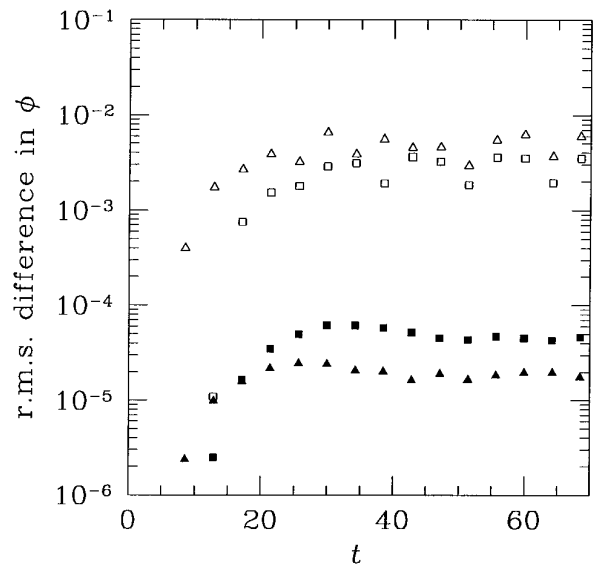


**FIGURE 14**

From the point of view of both computational cost and accuracy, matching appears to be a very effective way of solving free-space initial-value problems involving the three-dimensional scalar wave equation (1.1) with or without a nonlinear term. It is of course possible to achieve convergence with an ABC method applied to a nonlinear wave equation, by refining the grid *and simultaneously* enlarging the radius of the outer boundary. However, this is very expensive computationally, especially in the limit of small target error for the determination of waveforms in three-dimensional problems [44, 45]. Depending on the desired error limits, and on the strength and nature of the nonlinearities, various methods may or may not perform adequately. However, the matching method is convergent under grid refinement alone. Thus in the limit of small target error, the performance of the matching method is significantly better than that of any available alternative. Further, since the computational cost of the matching method is much lower than that of current nonlocal conditions, even when such a nonlocal condition is applicable it is much cheaper to use matching. In this way, higher resolutions and accuracies may be attained. In strongly nonlinear problems, matching appears to be the only available method which is able to produce numerical solutions which converge to the exact solution with a computational interface located at an arbitrary fixed position.

## APPENDIX A

### Quasi-Regular Triangulations of the Unit Sphere

A convenient first approximation to a quasi-regular triangulation of the unit sphere containing  $N_{\text{ang}}$  grid points may be obtained by randomly generating  $N_{\text{ang}}$  sets of spherical coordinates  $(\theta_i, \varphi_i)$  so that no two grid points are closer than a specified minimum angular separation  $\Delta_{\text{min}}$ . The value of  $\Delta_{\text{min}}$  should be smaller than, but as close as possible to, the average angular spacing  $\Delta$  between nearest neighbors in a quasi-regular triangulation. This latter quantity may be approximated by the empirical formula

$$\Delta \approx 3.59 N_{\text{ang}}^{-1/2}. \quad (\text{A1})$$

In practice, choosing  $\Delta_{\text{min}}$  too close to  $\Delta$  makes the random generation very time-consuming, since the area available for new grid points is rapidly exhausted. If  $\Delta_{\text{min}}/\Delta$  is chosen in the range 0.80–0.83, the random generation is fast, and the resulting set of angular grid points can already be used in matching algorithms.

Starting from a randomly generated triangulation, angular discretizations with a greater degree of uniformity may be obtained by an iterative process. To this end, we regard the angular grid points as a system of point particles which are constrained to move on the surface of the unit sphere,

**TABLE VI**

Generation of Triangulations with Average Angular Spacing  $\Delta \approx 0.092\lambda$

$\lambda$	$N_{\text{ang}}$	$\Delta_{\text{min}}/\lambda$	Initial Configuration		$T$	Final configuration	
			$\Delta/\lambda$	$\sigma_\Delta/\lambda$		$\Delta/\lambda$	$\sigma_\Delta/\lambda$
$\frac{4}{3}$	860	0.07500	0.07937	0.0046	0.45	0.08985	0.0026
1	1528	0.07500	0.07983	0.0046	0.45	0.09126	0.0026
$\frac{4}{5}$	2388	0.07338	0.07848	0.0051	0.60	0.09219	0.0027
$\frac{2}{3}$	3439	0.07500	0.07974	0.0048	0.15	0.09102	0.0027
$\frac{1}{2}$	6112	0.07460	0.07916	0.0048	0.15	0.09194	0.0028

*Note.* Equations (A2)–(A3) (with  $k = 0.1$ ,  $\varepsilon = 4$ ,  $\Lambda = 35$ ) are integrated from  $t = 0$  to  $t = T$  by an adaptive algorithm. The quantity  $\sigma_\Delta$  is the standard deviation of the angular separations (in radians) between neighboring grid points.

interacting with each other through a repulsive force law of the form

$$\mathbf{F}_{ij} = \frac{k}{r_{ij}^\varepsilon} (\mathbf{n}_i - \mathbf{n}_j),$$

where  $k$ ,  $\varepsilon > 0$  are constants,  $\mathbf{n}_i$  is the radius vector of the  $i$ th particle, and

$$r_{ij} = |\mathbf{n}_i - \mathbf{n}_j| = \sqrt{2(1 - \mathbf{n}_i \cdot \mathbf{n}_j)}^{1/2}$$

is the distance between particles  $i$  and  $j$ . In the presence of some dissipation, we intuitively expect that, for any choice of initial conditions, the particles will eventually approach an equilibrium distribution which very closely resembles a quasi-regular triangulation of the unit sphere. In spherical coordinates, the equations of motion of the system of particles may be written as

$$\ddot{\theta}_i - \frac{1}{2} \dot{\varphi}_i^2 \sin 2\theta_i + k \sum_{j \neq i} \frac{\mathbf{n}_j \cdot \boldsymbol{\theta}_i}{[2(1 - \mathbf{n}_i \cdot \mathbf{n}_j)]^{3/2}} + \Lambda \dot{\theta}_i = 0 \quad (\text{A2})$$

$$\ddot{\varphi}_i \sin \theta_i + 2\dot{\theta}_i \dot{\varphi}_i \cos \theta_i + k \sum_{j \neq i} \frac{\mathbf{n}_j \cdot \boldsymbol{\varphi}_i}{[2(1 - \mathbf{n}_i \cdot \mathbf{n}_j)]^{3/2}} + \Lambda \dot{\varphi}_i \sin \theta_i = 0, \quad (\text{A3})$$

where  $\boldsymbol{\theta}_i$  and  $\boldsymbol{\varphi}_i$  are the unit basis vectors of the spherical coordinate system at  $(\theta_i, \varphi_i)$  and  $\Lambda$  is a dissipation coefficient.

Using randomly generated triangulations as initial data, the above equations of motion may be integrated by an adaptive solver such as ODE [46] over a time interval  $O(\Lambda^{-1})$ , usually yielding an improved approximation to a quasi-regular triangulation. As an illustration of this procedure, we consider here the generation of the triangulations used in the numerical experiments of Subsection IV (Table VI). The average angular spacing  $\Delta$  of these triangulations



should be proportional to the parameter  $\lambda$  which measures the resolution of the computational grids; we have arbitrarily chosen a ratio  $\Delta/\lambda = 0.092$ . The second column of Table VI shows the required numbers of angular grid points, which have been computed using (A1). Using the random generation procedure with  $\Delta_{\min}/\Delta \simeq 0.81$ , we obtained the initial configurations described in the fourth and fifth columns of Table VI; subsequent integration of the equations of motion (A2)–(A3) led to the more uniform configurations described in the last two columns of Table VI.

## APPENDIX B

### Multiquadric Approximations

In  $d$  dimensions, the Hardy multiquadric interpolant to a function  $\psi(\mathbf{x}) = \psi(x^1, \dots, x^d)$  given on distinct data points  $\mathbf{x}_1, \dots, \mathbf{x}_M$  takes the form [33]

$$\psi_{\text{MQ}}(\mathbf{x}) = \sum_{\mu=1}^M a_{\mu} [s^2 + \|\mathbf{x} - \mathbf{x}_{\mu}\|^2]^{1/2}, \quad (\text{B1})$$

where the  $a_{\mu}$  are constants,  $\|\cdot\|$  denotes the Euclidean norm, and  $s$  is an arbitrary ‘‘shape parameter’’ [33], usually chosen to be of the order of the distances  $\|\mathbf{x}_{\mu} - \mathbf{x}_{\nu}\|$  between data points. The coefficients  $a_{\mu}$  are determined by solving the interpolation conditions  $\psi_{\text{MQ}}(\mathbf{x}_{\mu}) = \psi(\mathbf{x}_{\mu}) \equiv \psi_{\mu}$  ( $1 \leq \mu \leq M$ ). Alternatively, the value of the interpolant at a point  $\mathbf{x} = \bar{\mathbf{x}}$  may be expressed as

$$\psi_{\text{MQ}}(\bar{\mathbf{x}}) = \sum_{\mu=1}^M c_{\mu} \psi_{\mu}, \quad (\text{B2})$$

where the coefficients  $c_{\mu}$  are determined by the conditions

$$\sum_{\nu=1}^M A_{\mu\nu} c_{\nu} = b_{\mu}, \quad (\text{B3})$$

where

$$A_{\mu\nu} = [s^2 + \|\mathbf{x}_{\mu} - \mathbf{x}_{\nu}\|^2]^{1/2} \quad (\text{B4})$$

$$b_{\mu} = [s^2 + \|\bar{\mathbf{x}} - \mathbf{x}_{\mu}\|^2]^{1/2}. \quad (\text{B5})$$

Although this basic form of multiquadric interpolation often produces excellent results [34], its convergence properties are unsatisfactory. To see this, assume that the data points  $\mathbf{x}_{\mu}$  approach  $\bar{\mathbf{x}}$  according to

$$\mathbf{x}_{\mu} = \bar{\mathbf{x}} + \lambda \mathbf{v}_{\mu}, \quad (\text{B6})$$

where  $\lambda$  is a small positive parameter and the  $\mathbf{v}_{\mu}$  are constant vectors, and choose the shape parameter as

$$s = \sigma\lambda, \quad \sigma = \text{const.} \quad (\text{B7})$$

(this choice ensures that  $s$  is of the order of the distances between data points, and also prevents the ill-conditioning of the matrix  $A_{\mu\nu}$  which would occur if  $s/\lambda \rightarrow \infty$  as  $\lambda \rightarrow 0$ ). We first note that (B3)–(B7) imply that the  $c_{\mu}$  are independent of  $\lambda$ ; then, expanding  $\psi(\mathbf{x})$  in a Taylor series around  $\mathbf{x} = \bar{\mathbf{x}}$ , it is easy to see that the error in the multiquadric estimate of  $\psi(\bar{\mathbf{x}})$  is

$$\psi_{\text{MQ}}(\bar{\mathbf{x}}) - \psi(\bar{\mathbf{x}}) = \left( \sum_{\mu} c_{\mu} - 1 \right) \psi(\bar{\mathbf{x}}) + O(\lambda),$$

which in general approaches a small nonzero value as  $\lambda \rightarrow 0$ .

We now discuss a systematic procedure to increase the convergence rate of multiquadric approximations. First we observe that an interpolation formula with error  $O(\lambda)$  can be obtained simply by normalizing the coefficients  $c_{\mu}$ : if  $\hat{c}_{\mu} = c_{\mu}/\sum_{\nu} c_{\nu}$ , then

$$\sum_{\mu} \hat{c}_{\mu} \psi_{\mu} - \psi(\bar{\mathbf{x}}) = O(\lambda)$$

as  $\lambda \rightarrow 0$ . More generally, we seek to obtain higher-order interpolation formulas by applying (hopefully small) corrections  $\delta_{\mu}$  to the coefficients  $\hat{c}_{\mu}$ . Expanding  $\psi(\mathbf{x})$  about  $\mathbf{x} = \bar{\mathbf{x}}$ , the error in the new approximation may be written as

$$\begin{aligned} \sum_{\mu} (\hat{c}_{\mu} + \delta_{\mu}) \psi_{\mu} - \psi(\bar{\mathbf{x}}) &= \left( \sum_{\mu} \delta_{\mu} \right) \psi(\bar{\mathbf{x}}) \\ &+ \sum_{\mu} (\hat{c}_{\mu} + \delta_{\mu}) \sum_{n=1}^{\infty} \lambda^n \sum_{|\alpha|=n} \frac{\mathbf{v}_{\mu}^{\alpha}}{\alpha!} D^{\alpha} \psi(\bar{\mathbf{x}}), \end{aligned}$$

where  $\alpha = (\alpha_1, \dots, \alpha_d)$  is a multi-index,  $|\alpha| = \sum_i \alpha_i$ ,  $\alpha! = \prod_i \alpha_i!$ ,  $D^{\alpha} = \prod_i (\partial_i)^{\alpha_i}$ , and  $\mathbf{v}^{\alpha} = \prod_i (v^i)^{\alpha_i}$ . An approximation with error  $O(\lambda^{p+1})$  is obtained if we require that the corrections satisfy the equations

$$\sum_{\mu} \delta_{\mu} = 0 \quad (\text{B8})$$

$$\sum_{\mu} \mathbf{v}_{\mu}^{\alpha} (\hat{c}_{\mu} + \delta_{\mu}) = 0 \quad (1 \leq |\alpha| \leq p). \quad (\text{B9})$$

The order  $M_{p,d}$  of this linear system equals the dimension of the space of polynomials of degree  $\leq p$  in  $d$  variables. Here we restrict ourselves to situations where  $M > M_{p,d}$ , so that the system (B8)–(B9) does not have a unique solution. In order to modify the original multiquadric approxi-

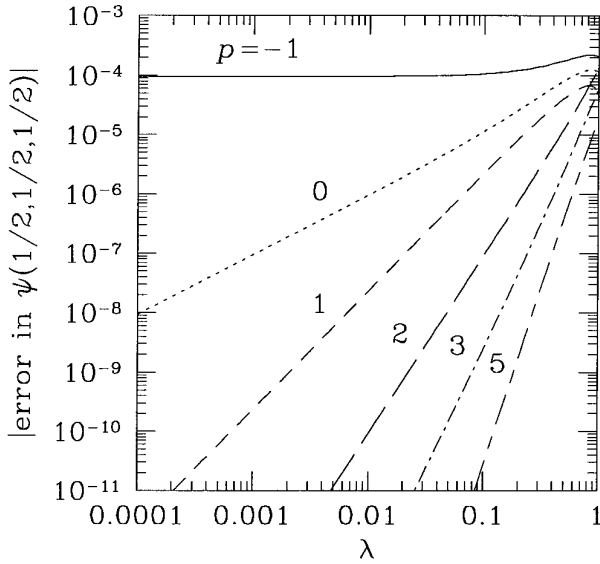


FIGURE 15

mation as little as possible, it is natural to choose  $\delta_\mu$  as the solution of the above system which minimizes the norm  $\sum_\mu \delta_\mu^2$ . It is straightforward to show that the solution of this minimization problem satisfies the system of  $M + M_{p,d}$  equations consisting of (B8)–(B9) and

$$\delta_\mu + \sum_{0 \leq |\alpha| \leq p} \mathbf{v}_\mu^\alpha \omega_\alpha = 0, \quad (\text{B10})$$

where the  $\omega_\alpha$  are Lagrange multipliers. Inserting (B10) in (B8)–(B9), we obtain the system of  $M_{p,d}$  equations

$$\sum_{0 \leq |\alpha| \leq p} \langle \mathbf{v}^{\beta+\alpha} \rangle \omega_\alpha = (1 - \delta_{|\beta|,0}) \langle \mathbf{v}^\beta \hat{c} \rangle \quad (0 \leq |\beta| \leq p), \quad (\text{B11})$$

where  $\langle \cdot \rangle$  denotes an average over  $\mu$  and  $\delta$  is Kronecker's delta. Once (B11) is solved for the Lagrange multipliers, the corrections  $\delta_\mu$  may be directly computed from (B10).

The above correction method can be readily generalized to approximations of derivatives  $D^\gamma \psi$ ,  $|\gamma| \geq 1$ . The simplest multiquadric approximation, obtained by differentiating the interpolant (B1), is given by

$$D^\gamma \psi(\bar{\mathbf{x}}) \approx \sum_\mu c_\mu \psi_\mu, \quad (\text{B12})$$

where  $c_\mu$  satisfies the system (B3) with  $b_\mu$  redefined as

$$b_\mu = D^\gamma [s^2 + \|\mathbf{x} - \mathbf{x}_\mu\|^2]^{1/2} |_{\mathbf{x}=\bar{\mathbf{x}}}. \quad (\text{B13})$$

When  $\mathbf{x}_\mu \rightarrow \bar{\mathbf{x}}$ , it is easy to see from (B3)–(B4), (B6)–(B7), and (B13) that  $c_\mu = \tilde{c}_\mu / \lambda^q$ , where  $q = |\gamma|$  and  $\tilde{c}_\mu$  is independent of  $\lambda$ ; therefore, the error in the approximation (B12)

is generally  $O(\lambda^{-q})$  as  $\lambda \rightarrow 0$ . A convergent approximation with error  $O(\lambda^{p-q+1})$  ( $p \geq q$ ) can be obtained by applying corrections  $\delta_\mu$  to the coefficients  $\tilde{c}_\mu$ , chosen so as to eliminate the coefficients of  $D^\alpha \psi(\bar{\mathbf{x}})$ ,  $0 \leq |\alpha| \leq p$ , in the Taylor expansion for the truncation error of the corrected approximation. If  $M \geq M_{p,d}$ , a slight modification of the previous analysis shows that the minimum-norm corrections are given by (B10), where the multipliers  $\omega_\alpha$  are now obtained by solving the system of  $M_{p,d}$  linear equations

$$\sum_{0 \leq |\alpha| \leq p} \langle \mathbf{v}^{\beta+\alpha} \rangle \omega_\alpha = \langle \mathbf{v}^\beta \hat{c} \rangle - \gamma! \delta_{\beta\gamma} / M \quad (0 \leq |\beta| \leq p).$$

To illustrate the effectiveness of the above correction scheme, we consider the approximation of the Gaussian function

$$\psi(x, y, z) = e^{-(x^2+y^2+z^2)} \quad (\text{B14})$$

and its derivative  $\partial_x^2 \psi$  at  $\bar{x} = \bar{y} = \bar{z} = \frac{1}{2}$  using  $M = 70$  data points. The vectors  $\mathbf{v}_\mu$  have been selected randomly inside the cubic region  $|v^i| \leq \frac{1}{2}$  ( $i = 1, 2, 3$ ), with the condition that  $\|\mathbf{v}_\mu - \mathbf{v}_\nu\| > 0.194$  for all  $\mu, \nu$ . Figures 15 and 16 show the behavior of the errors for the various approximations discussed above, with the shape parameter chosen as  $s = \frac{1}{2}\lambda$ . In most cases, the corrected approximations exhibit a substantial improvement over the uncorrected ones, with only minor changes in the coefficients  $c_\mu$  of the original multiquadric approximations.

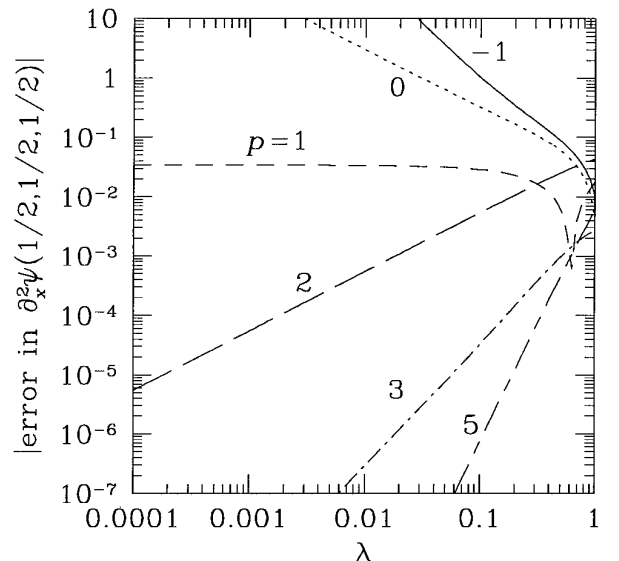


FIGURE 16

We now discuss the application of the above techniques to the generation of the interpolation and finite-difference formulas which are required by the matching schemes of Section III:

1. *Approximation of the operator  $L^2$ .* In order to evaluate  $L^2g$  at an angular grid point  $(\theta_\beta, \varphi_\beta)$  using the stencil (3.6), we consider a rotated spherical coordinate system  $(\theta', \varphi')$  such that  $\theta'_\beta = \pi/2$ ,  $\varphi'_\beta = 0$ . At this point, the operator  $L^2$  reduces to the simple form

$$L^2g = -(\partial_{\theta'\theta'}g + \partial_{\varphi'\varphi'}g),$$

so that the general correction scheme is applicable with  $d = 2$ ,  $\mathbf{x} = (\theta', \varphi')$ ,  $\bar{\mathbf{x}} = (\pi/2, 0)$ ,  $\psi = g$ ,  $M = N_L$ ,  $s = s_L$ ,  $\lambda = \Delta$ . The error in the corrected approximations is  $O(\Delta^{p-1})$ ; in the numerical experiments of Section IV we used  $N_L = 31$  and  $p = 3$ .

2. *Approximation of derivative  $\delta_{lq}^l g$ ,  $l = 1, 2$ ,  $q = x, y, z$ .* To generate finite-difference formulas for these derivatives, we begin by computing the Cartesian coordinates of the data points (3.12); the general correction scheme is then applicable with  $d = 3$ ,  $\mathbf{x} = (x, y, z)$ ,  $\bar{\mathbf{x}} = (x_i, y_j, z_k)$ ,  $\psi = g$ ,  $M = 5N_g$ ,  $s = s_g$ ,  $\lambda = \Delta\xi$  (it is assumed that  $\Delta/\Delta\xi = \text{const.}$  when  $\Delta\xi \rightarrow 0$ ). The error in the corrected approximation is  $O(\Delta^{p-l+1})$ ; in the numerical experiments of Section IV we used  $N_g = 20$ ,  $p = 4$ .

3. *Updating of boundary values for the exterior grid.* This is a three-dimensional interpolation problem which corresponds to the general correction scheme with  $d = 3$ ,  $\mathbf{x} = (x, y, z)$ ,  $\bar{\mathbf{x}} = (x_\beta, y_\beta, z_\beta)$ ,  $\psi = \phi$ ,  $M = N_B$ ,  $s = s_B$ ,  $\lambda = h$ . The error in the corrected approximations is  $O(h^{p+1})$ ; in the numerical experiments of Section IV we used  $N_B = 125$ ,  $p = 3$ .

## APPENDIX C

### An Exact Solution of the Forced Linear Wave Equation

When the source term  $S(r, t)$  has the structure (4.13)–(4.14), the forced solution represented by the Kirchhoff integral (4.12) can be evaluated in terms of elementary functions. The solution has different expressions in each of the following six regions of the  $(r, t)$  plane:

*Region I:*  $r \leq r_0$ ,  $t - r \geq r_0$

$$\begin{aligned} \phi(r, t) = & \frac{k}{2\omega^2(k^2 - \omega^2)} \frac{\sin \omega r}{r} \\ & \left\{ \pi \cos[\omega(t - r_0)] + \frac{k(k^2 - 3\omega^2)}{\omega(k^2 - \omega^2)} \sin[\omega(t - r_0)] \right\} \\ & + \left[ \frac{\cos kr}{2(k^2 - \omega^2)} - \frac{1}{2\omega^2} - \frac{k}{(k^2 - \omega^2)^2} \frac{\sin kr}{r} \right] \sin \omega t. \end{aligned}$$

*Region II:*  $r \geq r_0$ ,  $t - r \geq r_0$

$$\begin{aligned} \phi(r, t) = & \frac{k}{2\omega^2(k^2 - \omega^2)} \\ & \left[ \frac{k(k^2 - 3\omega^2)}{\omega(k^2 - \omega^2)} \sin \omega r_0 - \pi \cos \omega r_0 \right] \frac{\sin[\omega(t - r)]}{r}. \end{aligned}$$

*Region III:*  $r \geq r_0$ ,  $|t - r| \leq r_0$

$$\begin{aligned} \phi(r, t) = & \frac{r_0^2 - (t - r)^2}{8\omega r} + \frac{1}{4\omega r} \left( \frac{1}{\omega^2} - \frac{1}{k^2} \right) \\ & - \frac{k}{4\omega^2(k^2 - \omega^2)r} \left\{ \pi \sin[\omega(t - r + r_0)] \right. \\ & \left. + \frac{k(k^2 - 3\omega^2)}{\omega(k^2 - \omega^2)} \cos[\omega(t - r + r_0)] \right\} \\ & - \frac{\omega}{4k(k^2 - \omega^2)} \left\{ \left( 1 - \frac{t}{r} \right) \sin[k(t - r)] \right. \\ & \left. + \frac{(\omega^2 - 3k^2) \cos[k(t - r)]}{k(k^2 - \omega^2)} \frac{1}{r} \right\}. \end{aligned}$$

*Region IV:*  $r - t \geq r_0$

$$\phi(r, t) = 0.$$

*Region V:*  $r \leq r_0$ ,  $t + r \geq r_0$ ,  $t - r \leq r_0$

$$\begin{aligned} \phi(r, t) = & \frac{r_0^2 - (t - r)^2}{8\omega r} + \frac{1}{4\omega r} \left( \frac{1}{\omega^2} - \frac{1}{k^2} \right) \\ & + \frac{k}{4\omega^2(k^2 - \omega^2)r} \left\{ \pi \sin[\omega(t + r - r_0)] \right. \\ & \left. - \frac{k(k^2 - 3\omega^2)}{\omega(k^2 - \omega^2)} \cos[\omega(t + r - r_0)] \right\} \\ & - \frac{\omega}{4k(k^2 - \omega^2)} \left\{ \left( 1 - \frac{t}{r} \right) \sin[k(t - r)] \right. \\ & \left. + \frac{(\omega^2 - 3k^2) \cos[k(t - r)]}{k(k^2 - \omega^2)} \frac{1}{r} \right\} \\ & + \left[ \frac{\cos kr}{2(k^2 - \omega^2)} - \frac{1}{2\omega^2} - \frac{k}{(k^2 - \omega^2)^2} \frac{\sin kr}{r} \right] \sin \omega t. \end{aligned}$$

Region VI:  $t + r \leq r_0$

$$\begin{aligned} \phi(r, t) = & \frac{t}{2\omega} - \frac{\omega}{4k(k^2 - \omega^2)} \\ & \left\{ \left(1 - \frac{t}{r}\right) \sin[k(t - r)] + \left(1 + \frac{t}{r}\right) \sin[k(t + r)] \right\} \\ & - \frac{\omega(\omega^2 - 3k^2)}{2k^2(k^2 - \omega^2)^2} \frac{\sin kr}{r} \sin kt \\ & + \left[ \frac{\cos kr}{2(k^2 - \omega^2)} - \frac{1}{2\omega^2} - \frac{k}{(k^2 - \omega^2)^2} \frac{\sin kr}{r} \right] \sin \omega t. \end{aligned}$$

In the above equations, we have introduced the notation  $k = \pi/r_0$ , and assumed that  $S_0 = 1$ .

### ACKNOWLEDGMENTS

This work has been supported by the Binary Black Hole Grand Challenge Alliance, NSF PHY/ASC 9318152 (ARPA supplemented), by NSF PHY 9310083, by a Cray Research grant to R.A.M., and by NSF PHY 9510895 and NSF INT 9515257 to the University of Pittsburgh. N.T.B. thanks the Foundation for Research Development, South Africa, for financial support, and the University of Pittsburgh for hospitality during a sabbatical. P.R.H. has been supported by Fundação de Amparo à Pesquisa do Estado de São Paulo (São Paulo, Brazil) under Grant 93/5008-4. Computer time for this project has been provided by the Pittsburgh Supercomputing Center under Grant PHY860023P to J.W. and by the NSF MetaCenter Grant MCA94P015P, and a grant from the Center for High Performance Computing of the University of Texas at Austin, to R.A.M.

### REFERENCES

1. E. Lindman, *J. Comput. Phys.* **18**, 66 (1975).
2. M. Israeli and S. A. Orszag, *J. Comput. Phys.* **41**, 115 (1981).
3. R. Higdon, *Math. Comput.* **47**, 437 (1986).
4. R. Renaut, *J. Comput. Phys.* **102**, 236 (1992).
5. D. Givoli, *J. Comput. Phys.* **94**, 1 (1991).
6. S. V. Tsynkov, *Artificial Boundary Conditions Based on the Difference Potentials Method*. NASA Technical Memorandum No. 110265 (Langley Research Center, July 1996).
7. V. Ryaben'kii and S. V. Tsynkov, An application of the difference potentials method to solving external problems in CFD, NASA Technical Memorandum No. 110338 (Langley Research Center, March 1997).
8. B. Engquist and A. Majda, *Math Comput.* **31**, 629 (1977).
9. A. Bayliss and E. Turkel, *Commun. Pure Appl. Math.* **XXXIII**, 707 (1980).
10. L. Trefethen and L. Halpern, *Math. Comput.* **47**, 421 (1986).
11. J. Blaschak and G. Kriegsmann, *J. Comput. Phys.* **77**, 109 (1988).
12. H. Jiang and Y. S. Wong, *J. Comput. Phys.* **88**, 205 (1990).
13. L. Ting and M. Miksis, *J. Acoust. Soc. Am.* **80**, 1825 (1986).
14. J. de Moerloose and D. de Zutter, *IEEE Trans. Antennas Propagation* **41**, 890 (1993).
15. K. W. Thompson, *J. Comput. Phys.* **68**, 1 (1987).
16. G. W. Hedstrom, *J. Comput. Phys.* **30**, 222 (1979).
17. T. M. Hagstrom and S. Hariharan, *Math. Comput.* **581**, 51 (1988).
18. F. G. Friedlander, *The Wave Equation on a Curved Space-Time* (Cambridge Univ. Press, Cambridge, UK, 1975), Chap. 5, p. 193.
19. R. Gómez, J. Winicour, and R. Isaacson, *J. Comput. Phys.* **98**, 11 (1992).
20. R. Penrose, *Phys. Rev. Lett.* **10**, 66 (1963).
21. H. Friedrich and J. M. Stewart, *Proc. R. Soc. A* **385**, 345 (1983).
22. N. Bishop, in *Approaches to Numerical Relativity*, edited by R. d'Inverno (Cambridge Univ. Press, Cambridge, UK 1992).
23. N. Bishop, *Class. Quantum Grav.* **10**, 333 (1993).
24. C. Clarke and R. d'Inverno, *Class. Quantum Grav.* **11**, 1463 (1994).
25. N. T. Bishop *et al.*, *Phys. Rev. Lett.* **76**, 4303 (1996).
26. J. Anderson, *J. Comput. Phys.* **75**, 288 (1988).
27. J. L. Anderson and D. W. Hobill, in *Dynamical Spacetimes and Numerical Relativity*, edited by J. M. Centrella (Cambridge Univ. Press, Cambridge, UK, 1986).
28. R. Gómez, P. Laguna, P. Papadopoulos, and J. Winicour, *Phys. Rev. D* **54**, 4719 (1996).
29. C. Clarke, R. d'Inverno, and J. Vickers, *Phys. Rev. D* **52**, 6863 (1995).
30. M. Dubal, R. d'Inverno, C. Clarke, *Phys. Rev. D* **52**, 6868 (1995).
31. R. Gómez, L. Lehner, P. Papadopoulos, and J. Winicour, *Class. Quantum Grav.* **14**, 977 (1997).
32. P. Papadopoulos, Ph.D. thesis, University of Pittsburgh, 1994.
33. R. Hardy, *Comput. Math. Appl.* **19**, 163 (1990).
34. R. Franke, *Math Comput.* **38**, 381 (1982).
35. E. Kansa, *Comput. Math. Appl.* **19**, 147 (1990).
36. M. Dubal, *Phys. Rev. D* **45**, 1178 (1992).
37. G. Cook *et al.*, *Phys. Rev. D* **47**, 1471 (1993).
38. M. Buhmann and N. Dyn, in *Curves and Surfaces*, Edited by P.-J. Laurent, A. Le Méhauté, and L. Schumaker (Academic Press, New York, 1991).
39. M. Powell, in *Curves and Surfaces*, edited by P.-J. Laurent, A. Le Méhauté, and L. Schumaker (Academic Press, New York, 1991).
40. R. Carlson and T. Foley, *Comput. Math. Appl.* **21**, 29 (1991).
41. A. Mitchell and D. Griffiths, *The Finite Difference Method in Partial Differential Equations* (Wiley, Chichester, 1980).
42. L. Richardson, *Philos. Trans. R. Soc.* **210**, 307 (1910).
43. D. Zwillinger, *Handbook of Differential Equations* (Academic Press, San Diego, 1992).
44. N. Bishop, in *3rd Texas Workshop on 3-Dimensional Numerical Relativity*, edited by R. Matzner (Univ. of Texas, Austin, 1996).
45. N. Bishop, R. Gómez, L. Lehner, and J. Winicour, *Phys. Rev. D* **54**, 6153 (1996).
46. L. Shampine and M. Gordon, *Computer Solution of Ordinary Differential Equations: The Initial Value Problem* (Freeman, San Francisco, 1975).